

# Small-molecule inhibitors of human mitochondrial DNA transcription

<https://doi.org/10.1038/s41586-020-03048-z>

Received: 30 May 2019

Accepted: 22 October 2020

Published online: 16 December 2020

 Check for updates

Nina A. Bonekamp<sup>1,12</sup>, Bradley Peter<sup>2,12</sup>, Hauke S. Hillen<sup>3</sup>, Andrea Felser<sup>4</sup>, Tim Bergbrede<sup>5</sup>, Axel Choidas<sup>5</sup>, Moritz Horn<sup>6,7,8</sup>, Anke Unger<sup>5</sup>, Raffaella Di Lucrezia<sup>5</sup>, Ilian Atanassov<sup>9</sup>, Xiping Li<sup>9</sup>, Uwe Koch<sup>5</sup>, Sascha Menninger<sup>5</sup>, Joanna Boros<sup>5</sup>, Peter Habenberger<sup>5</sup>, Patrick Giavalisco<sup>10</sup>, Patrick Cramer<sup>3</sup>, Martin S. Denzel<sup>6</sup>, Peter Nussbaumer<sup>5</sup>, Bert Klebl<sup>5</sup>, Maria Falkenberg<sup>2</sup>, Claes M. Gustafsson<sup>2</sup> & Nils-Göran Larsson<sup>1,4,11</sup>

Altered expression of mitochondrial DNA (mtDNA) occurs in ageing and a range of human pathologies (for example, inborn errors of metabolism, neurodegeneration and cancer). Here we describe first-in-class specific inhibitors of mitochondrial transcription (IMTs) that target the human mitochondrial RNA polymerase (POLRMT), which is essential for biogenesis of the oxidative phosphorylation (OXPHOS) system<sup>1–6</sup>. The IMTs efficiently impair mtDNA transcription in a reconstituted recombinant system and cause a dose-dependent inhibition of mtDNA expression and OXPHOS in cell lines. To verify the cellular target, we performed exome sequencing of mutagenized cells and identified a cluster of amino acid substitutions in POLRMT that cause resistance to IMTs. We obtained a cryo-electron microscopy (cryo-EM) structure of POLRMT bound to an IMT, which further defined the allosteric binding site near the active centre cleft of POLRMT. The growth of cancer cells and the persistence of therapy-resistant cancer stem cells has previously been reported to depend on OXPHOS<sup>7–17</sup>, and we therefore investigated whether IMTs have anti-tumour effects. Four weeks of oral treatment with an IMT is well-tolerated in mice and does not cause OXPHOS dysfunction or toxicity in normal tissues, despite inducing a strong anti-tumour response in xenografts of human cancer cells. In summary, IMTs provide a potent and specific chemical biology tool to study the role of mtDNA expression in physiology and disease.

We used a high-throughput recombinant *in vitro* transcription assay system<sup>18</sup> to identify inhibiting compounds. A frontrunner compound (LDC195943; hereafter, IMT1) (Extended Data Fig. 1a, b) was developed and underwent additional hit-to-lead optimization for *in vivo* use in animals, which resulted in the pharmacologically improved lead compound LDC203974 (hereafter, IMT1B) (Fig. 1a). We performed a series of assays on IMT1 and IMT1B to assess their modes of action. Differential scanning fluorimetry showed that IMT1 and IMT1B stabilized POLRMT, causing large positive shifts in melting temperature ( $T_m$ ) (Fig. 1b, Extended Data Fig. 1c). We measured the steady-state kinetics of transcription using single-nucleotide incorporation assays (Fig. 1c, Extended Data Fig. 1d–f), which showed that addition of IMT1 or IMT1B markedly repressed the catalytic activity ( $V_{max,app}$ ) of POLRMT without major effects on the Michaelis constants ( $K_{Mapp}$ ) (Fig. 1c, Extended Data Fig. 1g). At concentrations greater than 100 nM, IMT1B progressively inhibited *in vitro* transcription from the mitochondrial light strand promoter (LSP) on linear and circular supercoiled templates (Fig. 1d, Extended Data Fig. 1h). Our microscale thermophoresis experiments

showed that IMT1B decreased the affinity of POLRMT to a DNA–RNA scaffold<sup>6</sup>, as the  $K_M$  increased from about 100 nM to around 750 nM (Fig. 1e, Extended Data Fig. 1i, j). Taken together, our biochemical data show that the IMT1 and IMT1B are noncompetitive inhibitors that cause a conformational change of POLRMT, which blocks substrate binding and transcription in a dose-dependent way *in vitro*.

## Inhibition of cellular mtDNA expression

We found that IMT1 and IMT1B caused a dose-dependent decrease in the levels of mitochondrial transcripts (Fig. 1f, Extended Data Fig. 2a) and gradual depletion of mtDNA (Fig. 1g, Extended Data Fig. 2b) in HeLa cells. We also observed a dose-dependent decrease in the levels of subunits (NDUFB8, UQCRC2 and COXI) of respiratory chain complexes I, III and IV, the stability of which depends on subunits encoded by mtDNA; by contrast, subunits (SDHB and ATP5A) of the exclusively nucleus-encoded complex II and F1 subcomplex of ATP synthase remained unchanged (Fig. 1h, Extended Data Fig. 2c). Consistent with these results, our

<sup>1</sup>Department of Mitochondrial Biology, Max Planck Institute for Biology of Ageing, Cologne, Germany. <sup>2</sup>Department of Medical Biochemistry and Cell Biology, University of Gothenburg, Gothenburg, Sweden. <sup>3</sup>Department of Molecular Biology, Max Planck Institute for Biophysical Chemistry, Göttingen, Germany. <sup>4</sup>Department of Medical Biochemistry and Biophysics, Karolinska Institutet, Stockholm, Sweden. <sup>5</sup>Lead Discovery Center, Dortmund, Germany. <sup>6</sup>Metabolic and Genetic Regulation of Ageing, Max Planck Institute for Biology of Ageing, Cologne, Germany. <sup>7</sup>Acus Laboratories, Cologne, Germany. <sup>8</sup>JLP Health, Vienna, Austria. <sup>9</sup>Proteomics Core Facility, Max Planck Institute for Biology of Ageing, Cologne, Germany. <sup>10</sup>Metabolomics Core Facility, Max Planck Institute for Biology of Ageing, Cologne, Germany. <sup>11</sup>Max Planck Institute for Biology of Ageing–Karolinska Institutet Laboratory, Karolinska Institutet, Stockholm, Sweden. <sup>12</sup>These authors contributed equally: Nina A. Bonekamp, Bradley Peter. <sup>✉</sup>e-mail: claes.gustafsson@medkem.gu.se; nils-goran.larsson@ki.se

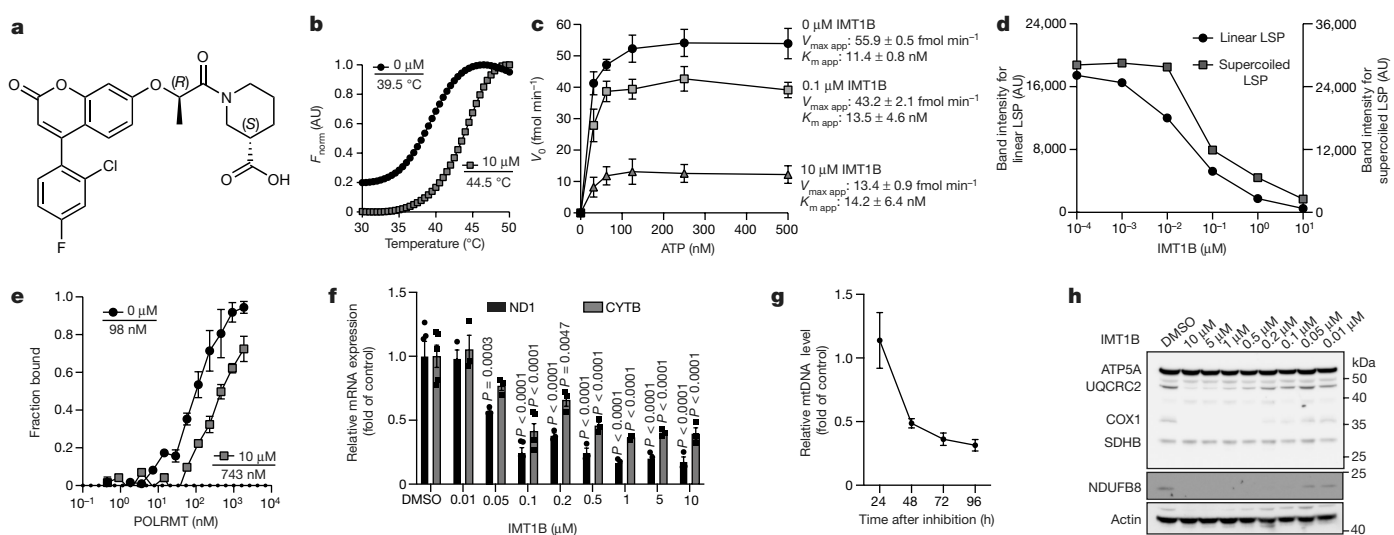


**Fig. 1 | IMTs affect stability, substrate binding and enzyme activity of POLRMT and inhibit mitochondrial gene expression.** **a**, Chemical structure of IMT1B (LDC203974). **b**, Differential scanning fluorimetry performed in the absence or presence of 10  $\mu$ M IMT1B ( $n=2$  independent experiments). The means of the determined melting temperatures are given.  $F_{\text{norm}}$ , normalized fluorescence; AU, arbitrary units. **c**, Single nucleotide incorporation assays at varying ATP concentrations in the presence of 0–10  $\mu$ M IMT1B (mean  $\pm$  s.d.,  $n=3$  independent experiments).  $V_{\text{max app}}$ , maximum reaction rate;  $K_{\text{m app}}$ , substrate affinity. **d**, Quantification of in vitro promoter-dependent transcription on linear LSP and supercoiled circular LSP templates in the

presence of 0–10  $\mu$ M IMT1B. The mean of  $n=2$  independent experiments is shown. **e**, Microscale thermophoresis binding curves in the absence or presence of 10  $\mu$ M IMT1B (mean  $\pm$  s.d.,  $n=3$  independent experiments). The determined  $K_d$  values are given. **f**, Mitochondrial transcript levels of ND1 and CYTB after IMT1B treatment for 6 h in HeLa cells (mean  $\pm$  s.e.m.;  $n=3$ –5 biological replicates; two-way analysis of variance (ANOVA) with Sidak's test for multiple comparisons, DMSO–IMT1B). **g**, mtDNA levels after IMT1B treatment (mean  $\pm$  s.e.m.,  $n=3$ –4 biological replicates). **h**, Immunoblot analysis of OXPHOS protein levels after IMT1B treatment (4 d, 30  $\mu$ g per lane). A representative image of  $n=2$  independent experiments is shown.

quantitative proteomics analysis of IMT1-treated A2780 ovarian carcinoma cells revealed a rapid progressive decrease in the levels of subunits of complexes I, III and IV (Extended Data Fig. 2d). Levels of cytosolic ribosomal proteins remained unaffected after 24 h of treatment with IMT1, whereas the levels of mitoribosomal proteins were severely depleted—which is consistent with the lack of 12S and 16S ribosomal RNA encoded by mtDNA (Extended Data Fig. 2d). As a consequence of the impaired mtDNA expression, basal respiration was significantly decreased in intact HeLa cells exposed to IMT1 (Extended Data Fig. 2e). IMT1 and IMT1B showed very similar patterns of mtDNA transcription inhibition in HeLa and A2780 cells, which demonstrates that the compounds have comparable effects in vitro (Extended Data Fig. 2f).

We performed single-nucleotide incorporation assays and found that IMT1B did not inhibit budding yeast mitochondrial RNA polymerase (RPO41), bacteriophage T7 RNA polymerase, *Escherichia coli* RNA polymerase or a reverse transcriptase (Extended Data Fig. 3a–d). In addition, IMT1B did not inhibit the human multi-subunit RNA polymerase II (RNA Pol II) in vitro (Extended Data Fig. 3e) and had no effect on RNA Pol I-, II- and III-dependent transcript levels in cell lines (Extended Data Fig. 3f). Furthermore, IMT1B did not inhibit human mitochondrial DNA polymerase  $\gamma$  in vitro or mitochondrial protein synthesis in organello (Extended Data Fig. 3g, h). As an independent control, we used SC-6238532 (con IMT)—a compound that is structurally related to IMTs—and found that it neither binds POLRMT nor affects mtDNA expression (Extended Data Fig. 3i–p). We thus conclude that IMT1 and IMT1B are highly specific inhibitors of POLRMT.

## IMTs selectively target POLRMT in cells

To determine the *in vivo* target of IMTs, we performed an unbiased genome-wide forward genetic screen<sup>19</sup> in A2780 cells (Extended Data Fig. 4a). We exposed the cells to a mutagen and treated them with a wild-type lethal dose of an IMT1 analogue. Exome sequencing of resistant clones revealed *POLRMT* mutations as the only candidate suppressors

of IMT toxicity. In total, we identified six independent point mutations in *POLRMT*, causing four amino acid substitutions (L796Q, F813L, L816Q and A821V, A821S or A821Q) clustered in the same region of the POLRMT protein (Fig. 2a). We expressed and purified recombinant mutant forms of POLRMT and found that addition of 10  $\mu$ M IMT1B did not result in any thermal shift of POLRMT mutants, consistent with impaired IMT1B binding (Fig. 2b). Furthermore, increasing concentrations of IMT1B did not inhibit transcription with the mutant recombinant versions of POLRMT (Extended Data Fig. 4b–f). A2780 cells genetically engineered to express POLRMT with the L796Q or L816Q substitutions (Extended Data Fig. 4g) displayed strong resistance to IMT1 in cell proliferation assays (Fig. 2c). Treatment with IMT1 severely impaired mtDNA gene expression in A2780 cells that express wild-type POLRMT, whereas cells that express mutant POLRMT (L796Q or L816Q) were resistant (Extended Data Fig. 4h). Together, these data demonstrate that POLRMT is the *in vivo* target of IMT1.

## Cryo-EM structure of POLRMT with IMT1B

We determined the structure of POLRMT in the presence of IMT1B by single-particle cryo-electron microscopy (Extended Data Fig. 5, Supplementary Table 1). The resulting reconstruction showed an average resolution of 3.5 Å, and allowed unambiguous docking and adjustment of a previous crystal structure of POLRMT<sup>6</sup>. Structural comparisons showed that the overall architecture of the enzyme was unchanged. Whereas the orientation of the N-terminal and pentatricopeptide (PPR) domains relative to the catalytic core resembled that observed in a previously published antitermination complex with POLRMT bound to mitochondrial transcription elongation factor (TEFM)<sup>20</sup>, the fingers domain involved in catalysis adopted a ‘clenched’ conformation as was previously observed in the free POLRMT crystal structure<sup>5</sup>.

We observed an additional density that was in good agreement with the shape and the chemical nature of the IMT1B molecule (Fig. 2d). Consistent with the location of resistance mutations identified in the forward genetic screen (Fig. 2a, d), the structural analysis showed that

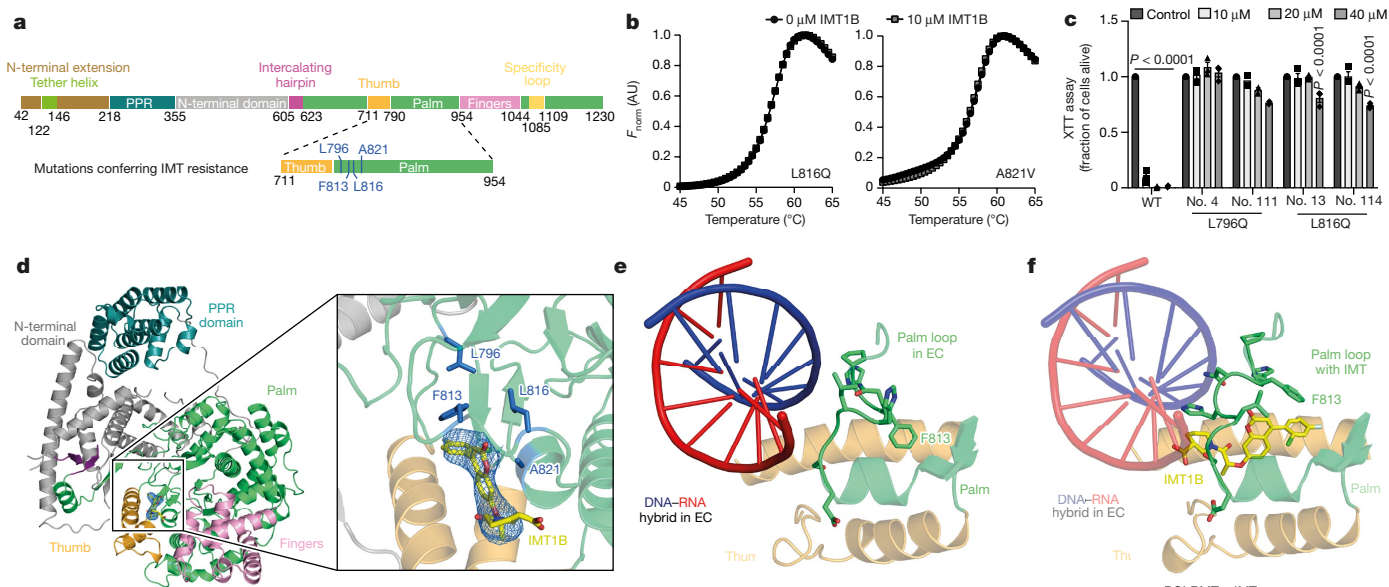


**Fig. 2 | POLRMT is the in vivo target of IMTs.** **a**, Schematic of the human POLRMT amino acid sequence (modified after a previous publication<sup>30</sup>). Residues that confer resistance to IMT upon mutation are highlighted in blue. **b**, Differential scanning fluorimetry performed in the absence and presence of 10  $\mu\text{M}$  IMT1B using the indicated POLRMT mutants ( $n = 2$  independent experiments). **c**, XTT assay after treatment of A2780 cells expressing IMT-resistant POLRMT mutations (2 clones each; denoted by different numbers) and wild-type (WT) controls (mean  $\pm$  s.e.m.,  $n = 3$  biological replicates (no. 111,  $n = 2$ ), two-way ANOVA with Sidak's test for multiple comparisons, control–IMT). Control denotes control treatment (DMSO). **d**, Cartoon representation of the cryo-EM structure of POLRMT bound to IMT1B. The cryo-EM density for IMT1B is shown as blue mesh. Inset shows a close-up view of the binding site of IMT1B between the thumb and palm domains of POLRMT. Residues identified as conferring resistance to IMT are shown as

sticks in blue. **e**, Structure of the palm loop in the mitochondrial transcription elongation complex (EC) (Protein Data Bank (PDB) code 5OLA)<sup>20</sup>. Parts of the thumb and palm domain are shown as translucent cartoon. The palm loop is shown as sticks. The DNA–RNA hybrid duplex in the active site is shown as a cartoon, and the RNA and template DNA are coloured in red and blue, respectively. **f**, Structure of the palm loop in the presence of IMT1B. Parts of the thumb and palm domain are shown as translucent cartoons. The palm loop is shown as sticks. The DNA–RNA hybrid duplex of the elongation complex was overlaid by aligning the structure of the elongation complex (PDB code 5OLA)<sup>20</sup> with the structure of POLRMT bound to IMT1B (residues 650–1230) and is shown as a translucent cartoon, coloured as in **e**. IMT1B binds to a hydrophobic pocket occupied by F813 in the palm loop in the elongation complex. The position of the palm loop observed in the POLRMT–IMT1B structure would clash with the RNA and template DNA in the elongation complex.

IMT1B binds between the base of the thumb and the palm domains of POLRMT (Fig. 2e, Extended Data Fig. 5d). The binding is accompanied and enabled by a rearrangement of a protein loop in the palm (the 'palm loop'; residues 811–819), which adopts a different conformation than in all previously reported structures of POLRMT<sup>5,6,20,21</sup> (Fig. 2d–f). In particular, IMT1B binds to a hydrophobic pocket that is otherwise occupied by residue F813 of the palm loop, excluding this amino acid residue from this location (Fig. 2e, f). The structure further shows that three of the four residues that confer resistance upon mutation (Fig. 2a) are within 4 Å distance of IMT1B, and predicts that the mutations would disrupt interactions (F813L), cause steric clashes (A821V) or render the hydrophobic pocket partially hydrophilic (L796Q or L816Q) (Fig. 2d).

The structure also suggests a possible mechanism of transcription inhibition by IMT1B. By comparing POLRMT in its free form<sup>5</sup>, the form of the initiation complex<sup>21</sup> and in pre- and post-translocated elongation complexes<sup>6,20</sup>, we found that the thumb and palm regions involved in IMT binding adopt virtually identical conformations. However, superpositions show that the rearrangement of the palm loop caused by IMT1B binding leads to clashes of the loop with the template DNA strand and the nascent RNA (Fig. 2e, f). These observations confirm that IMT1B acts as an allosteric inhibitor of POLRMT and indicate that inhibitor binding displaces the palm loop, which then sterically impairs binding of the DNA–RNA hybrid and translocation of the nascent RNA.

## Inhibition of cancer cell proliferation

Fast-growing tumour cells require mitochondrial metabolism<sup>9,14,22</sup>, and tumours and tumour stem cells are often highly dependent on OXP

HOS<sup>7,10–13,15,16,23</sup>. Consistent with chemical inhibition of POLRMT, silencing of *POLRMT* using short interfering RNA also leads to a decrease in cell growth<sup>124</sup> (Extended Data Fig. 6a, b). We undertook a large-scale cell viability assay that encompassed 89 cancer cell lines and primary cells (IMR90 lung fibroblasts and human peripheral blood mononuclear cells (PBMCs)), which showed a strong decrease in cell viability after IMT1 treatment in about one third of the cancer cell lines (whereas primary cells remained unresponsive) (Extended Data Fig. 6c). Sensitivity to IMT1 was not in any obvious way correlated with the tissue origin of the cancer cell line. We observed a dose-dependent decrease in cell viability in A2780, A549 and HeLa cells (Fig. 3a, Extended Data Fig. 6d), but—importantly—treatment with IMT1 was not cytotoxic to human PBMCs or pooled primary human hepatocytes (Extended Data Fig. 6e). Prolonged treatment with an IMT thus specifically affects the proliferation of cancer cells, which suggests that cancer therapy may be a potential in vivo application of IMTs.

## IMT treatment depletes cellular metabolites

Next, we investigated the basis of the observed cellular toxicity. Previous studies have identified the production of reactive oxygen species after inhibition of mitochondrial function as the cause of cell death<sup>23</sup>; however, we could not detect any substantial increase in reactive oxygen species over time (Extended Data Fig. 7a). We also did not detect increased PARP cleavage (Extended Data Fig. 7b) or upregulation of the pro-apoptotic, one-carbon, stress and degradation pathways by quantitative proteomics (Extended Data Fig. 7c). However, our analyses of steady-state polar metabolites in A2780 cells treated with IMT (Fig. 3b) revealed a time-dependent and marked increase in the levels

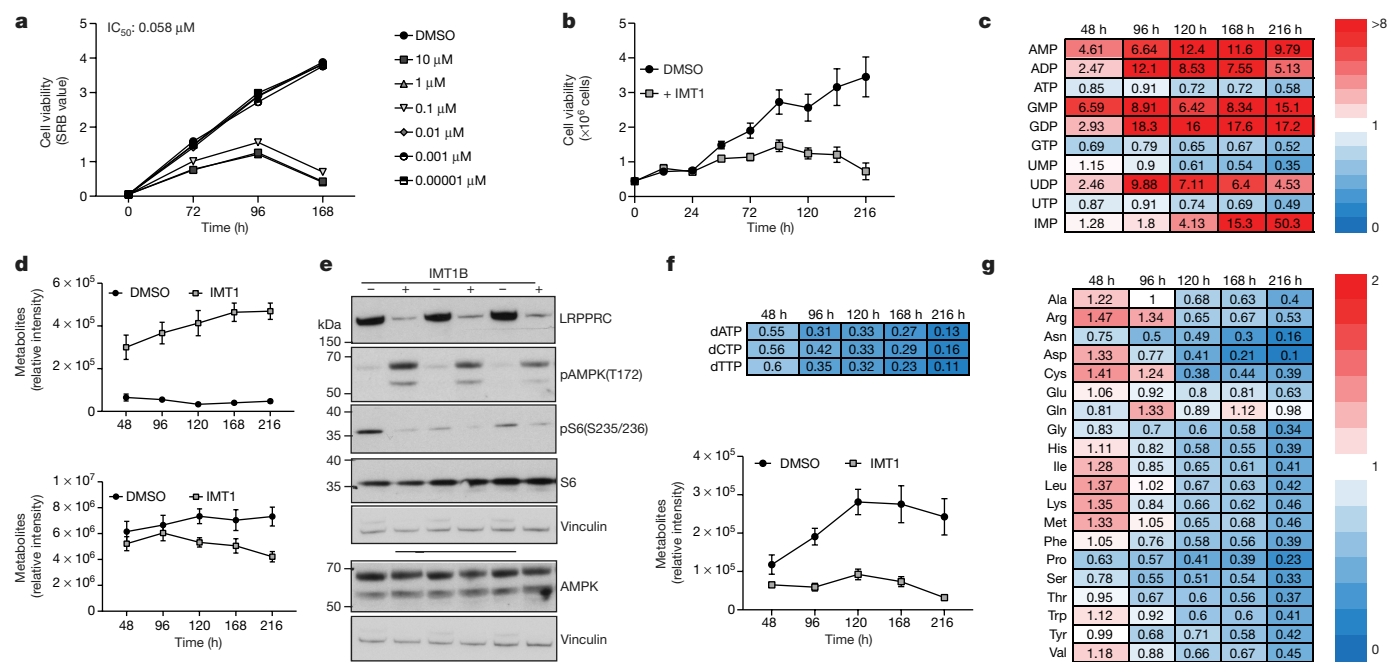


**Fig. 3 | IMTs specifically inhibit proliferation of cancer cells.**

**a**, Dose-dependent decrease in A2780 cell proliferation after IMT1 treatment (sulforhodamine B (SRB) assay). **b**, Time-dependent decrease in A2780 cell viability after IMT1 treatment (ViCell Cell Counter, mean  $\pm$  s.e.m.,  $n=4\text{--}5$  biological replicates). **c**, Fold changes in nucleotide levels after IMT1 treatment. Levels of nucleotides at different time points are expressed as fold of control (mean IMT1/control,  $n=5$  biological replicates). **d**, Metabolite levels of AMP (top) and ATP (bottom) are plotted in detail over time (mean  $\pm$  s.e.m.,  $n=4\text{--}5$  biological replicates). **e**, Immunoblot analysis of levels of AMPK phosphorylated at T172 (pAMPK(T172)) and ribosomal S6 phosphorylated at

S235 and S236 (pS6(S235/236)). For determination of total AMPK levels, samples were run on a separate gel and processed in parallel (20  $\mu$ g per lane). A representative image of  $n=3$  independent experiments is shown. **f**, Fold changes of dNTP levels after IMT1 treatment. Top, dNTP levels at different time points are expressed as fold of control (mean IMT1/control). Bottom, metabolite levels of dATP are plotted in detail over time (mean  $\pm$  s.e.m.,  $n=4\text{--}5$  biological replicates). **g**, Fold changes in amino acid levels after IMT1 treatment. Amino acid levels at different time points are expressed as fold of control. In the heat maps, dark blue is the minimum and dark red is the maximum; the range is given in the figure.

of mono- and diphosphate nucleotides that resulted in a considerable increase in the AMP/ATP ratio (Fig. 3c, d) and levels of phosphorylated AMPK (Fig. 3e). These observations are indicative of a cellular energy crisis, as expected from a nonfunctional OXPHOS system. Besides ATP production, mitochondrial metabolism provides a variety of metabolic intermediates for the generation of nucleotides and amino acids (Extended Data Fig. 7d). After 48 h, dATP levels in cells treated with IMT1 were decreased to 55% of control values, dropping to only 13% after 216 h. This difference is explained by the strong increase in dATP levels that occurs in control cells treated with dimethylsulfoxide (DMSO) over time—this is consistent with ongoing synthesis, which cannot occur in cells treated with IMT1 (Fig. 3f). We observed a similar pattern for levels of dCTP and dTTP (Fig. 3f), as well as a time-dependent decrease of citric-acid-cycle intermediates (Extended Data Fig. 7d) that resulted in a marked depletion of cellular amino acid levels over time (Fig. 3g). Treatment with IMT1 thus puts the cell into a state of severe energy and nutrient depletion. The loss of necessary cellular building blocks cannot be compensated for and leads to reduced cellular proliferation (Fig. 3b), as supported by our finding of a reduction in the levels of the cellular proliferation marker PCNA (Extended Data Fig. 7e) and levels of phosphorylated S6 ribosomal protein (Fig. 3e). Immunoblot analysis revealed that both DMSO- and IMT1-treated cells were positive for cleaved PARP in the supernatant, indicating eventual apoptotic cell death (Extended Data Fig. 7b). The total number of dead cells after prolonged treatment with an IMT was strongly increased compared to controls.

## Inhibition of tumour growth without toxicity

Because IMTs affect the growth of cancer cells without affecting control cells (Extended Data Fig. 6c), we orally treated mice containing human

A2780 or DLD-1 cancer cell xenografts with IMT1B (Fig. 4, Extended Data Fig. 8). The IMT1B *in vivo* pharmacokinetic parameters (Extended Data Fig. 8a, b) allowed a single oral dose per day. Importantly, mouse POLRMT is sensitive to IMT1B treatment to a similar degree to human POLRMT, according to our differential scanning fluorimetry and *in vitro* transcription assays (Extended Data Fig. 8c, d). The application of 100 mg of IMT1B per kg body weight led to a clear reduction of tumour volume (Fig. 4a, Extended Data Fig. 8e, f). Treated mice showed a nonsignificant tendency towards a slightly lower body weight (Extended Data Fig. 8g). We observed no signs of acute or chronic liver or kidney toxicity (Extended Data Fig. 8h) and no induction of anaemia, thrombocytopenia or leukopenia (Extended Data Fig. 8i) after the treatment of wild-type mice with IMT1B for four weeks at a dose sufficient to reduce tumour size in mice containing xenografts.

On a molecular level, the treatment of mice with IMT1B reduced mtDNA transcript levels and respiratory-chain subunit levels in tumours (Fig. 4b, c), whereas mitochondrial transcripts in differentiated tissues were reduced to a lesser extent (Fig. 4b) and OXPHOS protein levels remained normal in liver and heart (Fig. 4c). The levels of mtDNA showed a slight, nonsignificant decrease in tumours, whereas there were no changes in liver and heart (Extended Data Fig. 8j). The observation that treatment with an IMT causes mtDNA depletion in HeLa cells but not in xenograft tumours is probably explained by the very fast cell division of HeLa cells in tissue culture. Treatment with IMT1B *in vivo* caused an upregulation of phosphorylated AMPK and a decrease in phosphorylated ribosomal S6 protein in tumour tissue (Extended Data Fig. 8k), although this was not as extreme as in tissue-culture cells (Fig. 3e).

The finding that treatment with IMT1B for up to four weeks is very well-tolerated in the mouse is consistent with previous genetic

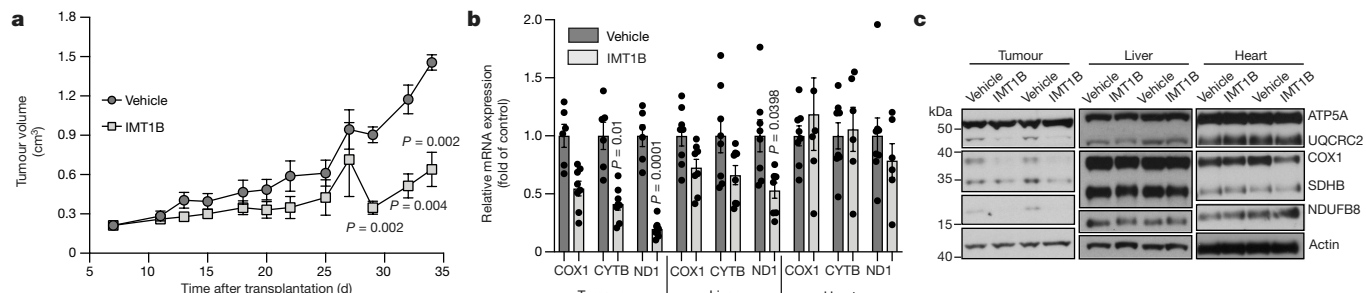


**Fig. 4 | IMT treatment inhibits tumour growth in vivo and mitochondrial gene expression in a dose-dependent manner.** **a,** Growth of A2780 xenograft tumours in vivo. Mice were treated once per day with either vehicle or IMT1B (100 mg per kg body weight). Mean  $\pm$  s.e.m.;  $n=8$  or 6 (after day 27) biological replicates, Mann–Whitney *U*-test, exact significance, one-tailed, vehicle–IMT1B. **b,c,** IMT1B treatment affects mitochondrial gene expression in a tissue-specific manner. **b,** Mitochondrial transcript levels (mtRNA) in vehicle-

and IMT-treated tumour, liver and heart (mean  $\pm$  s.e.m.; tumour vehicle-treated and heart IMT-treated group:  $n=6$  biological replicates, other groups:  $n=8$  biological replicates, two-way ANOVA, Sidak's multiple comparisons test, vehicle–IMT1B). **c,** Mitochondrial protein levels in tumour, liver and heart were determined by immunoblotting of OXPHOS proteins (50  $\mu$ g per lane). A representative image of  $n=3$  independent experiments is shown.

experiments that have shown that loss of mtDNA expression can be tolerated for a very long time in post-mitotic tissues<sup>25–28</sup>, although disruption in the germ line results in embryonic lethality<sup>3,29</sup>. These findings underscore the critical importance of mtDNA expression for biogenesis of the OXPHOS system in rapidly dividing cells, and explain why disruption of mtDNA gene expression can have substantial anti-tumour effects without affecting normal tissues.

In conclusion, IMTs are first-in-class, potent and highly specific allosteric inhibitors of POLRMT, which is essential for mtDNA transcription. The IMTs show potent effects for the treatment of cancer in preclinical mouse models and have the potential to be further developed for clinical applications in human cancer. In addition, IMTs represent a potent chemical biology tool for manipulating mtDNA transcription—and thereby OXPHOS capacity—in a dose-dependent way in animal models to assess how the downregulation of OXPHOS affects a variety of physiological and disease processes relevant for human health.

## Online content

Any methods, additional references, Nature Research reporting summaries, source data, extended data, supplementary information, acknowledgements, peer review information; details of author contributions and competing interests; and statements of data and code availability are available at <https://doi.org/10.1038/s41586-020-03048-z>.

- Kühl, I. et al. POLRMT does not transcribe nuclear genes. *Nature* **514**, E7–E11 (2014).
- Kühl, I. et al. Transcriptomic and proteomic landscape of mitochondrial dysfunction reveals secondary coenzyme Q deficiency in mammals. *elife* **6**, e30952 (2017).
- Kühl, I. et al. POLRMT regulates the switch between replication primer formation and gene expression of mammalian mtDNA. *Sci. Adv.* **2**, e1600963 (2016).
- Posse, V. et al. The amino terminal extension of mammalian mitochondrial RNA polymerase ensures promoter specific transcription initiation. *Nucleic Acids Res.* **42**, 3638–3647 (2014).
- Ringel, R. et al. Structure of human mitochondrial RNA polymerase. *Nature* **478**, 269–273 (2011).
- Schwinghammer, K. et al. Structure of human mitochondrial RNA polymerase elongation complex. *Nat. Struct. Mol. Biol.* **20**, 1298–1303 (2013).
- Birsoy, K. et al. Metabolic determinants of cancer cell sensitivity to glucose limitation and biguanides. *Nature* **508**, 108–112 (2014).
- Bosc, C., Selak, M. A. & Sarry, J. E. Resistance is futile: targeting mitochondrial energetics and metabolism to overcome drug resistance in cancer treatment. *Cell Metab.* **26**, 705–707 (2017).
- Funes, J. M. et al. Transformation of human mesenchymal stem cells increases their dependency on oxidative phosphorylation for energy production. *Proc. Natl Acad. Sci. USA* **104**, 6223–6228 (2007).
- Kuntz, E. M. et al. Targeting mitochondrial oxidative phosphorylation eradicates therapy-resistant chronic myeloid leukemia stem cells. *Nat. Med.* **23**, 1234–1240 (2017).
- Lee, J. et al. Effective breast cancer combination therapy targeting BACH1 and mitochondrial metabolism. *Nature* **568**, 254–258 (2019).
- Shi, Y. et al. Gboxin is an oxidative phosphorylation inhibitor that targets glioblastoma. *Nature* **567**, 341–346 (2019).
- Škrčík, M. et al. Inhibition of mitochondrial translation as a therapeutic strategy for human acute myeloid leukemia. *Cancer Cell* **20**, 674–688 (2011).
- Vander Heiden, M. G. & DeBerardinis, R. J. Understanding the intersections between metabolism and cancer biology. *Cell* **168**, 657–669 (2017).
- Viale, A. et al. Oncogene ablation-resistant pancreatic cancer cells depend on mitochondrial function. *Nature* **514**, 628–632 (2014).
- Martinez-Reyes, I. et al. Mitochondrial ubiquinol oxidation is necessary for tumour growth. *Nature* **585**, 288–292 (2020).
- Vasan, K., Werner, M. & Chandel, N. S. Mitochondrial metabolism as a target for cancer therapy. *Cell Metab.* **32**, 341–352 (2020).
- Bergbrede, T., Hoberg, E., Larsson, N. G., Falkenberg, M. & Gustafsson, C. M. An adaptable high-throughput technology enabling the identification of specific transcription modulators. *SLAS Discov.* **22**, 378–386 (2017).
- Horn, M. et al. Unbiased compound-protein interface mapping and prediction of chemoresistance loci through forward genetics in haploid stem cells. *Oncotarget* **9**, 9838–9851 (2018).
- Hillen, H. S. et al. Mechanism of transcription anti-termination in human mitochondria. *Cell* **171**, 1082–1093 (2017).
- Hillen, H. S., Morozov, Y. I., Sarfallah, A., Temiakov, D. & Cramer, P. Structural basis of mitochondrial transcription initiation. *Cell* **171**, 1072–1081 (2017).
- Srisankathadevan, S. et al. AML cells have low spare reserve capacity in their respiratory chain that renders them susceptible to oxidative metabolic stress. *Blood* **125**, 2120–2130 (2015).
- Weinberg, F. et al. Mitochondrial metabolism and ROS generation are essential for Kras-mediated tumorigenicity. *Proc. Natl Acad. Sci. USA* **107**, 8788–8793 (2010).
- Bralha, F. N. et al. Targeting mitochondrial RNA polymerase in acute myeloid leukemia. *Oncotarget* **6**, 37216–37228 (2015).
- Wang, J. et al. Dilated cardiomyopathy and atrioventricular conduction blocks induced by heart-specific inactivation of mitochondrial DNA gene expression. *Nat. Genet.* **21**, 133–137 (1999).
- Sørensen, L. et al. Late-onset corticohippocampal neurodepletion attributable to catastrophic failure of oxidative phosphorylation in MILON mice. *J. Neurosci.* **21**, 8082–8090 (2001).
- Viader, A. et al. Schwann cell mitochondrial metabolism supports long-term axonal survival and peripheral nerve function. *J. Neurosci.* **31**, 10128–10140 (2011).
- Wredenberg, A. et al. Increased mitochondrial mass in mitochondrial myopathy mice. *Proc. Natl Acad. Sci. USA* **99**, 15066–15071 (2002).
- Larsson, N. G. et al. Mitochondrial transcription factor A is necessary for mtDNA maintenance and embryogenesis in mice. *Nat. Genet.* **18**, 231–236 (1998).
- Hillen, H. S., Temiakov, D. & Cramer, P. Structural basis of mitochondrial transcription. *Nat. Struct. Mol. Biol.* **25**, 754–765 (2018).

**Publisher's note** Springer Nature remains neutral with regard to jurisdictional claims in published maps and institutional affiliations.

© The Author(s), under exclusive licence to Springer Nature Limited 2020

## Methods

Statistical analysis was performed to predetermine the sample sizes for xenograft studies. For xenograft experiments, toxicity panels and pharmacokinetic analysis, randomization of experimental groups was performed. Investigators were not blinded during experiments and outcome assessment.

### IMTs

The details of the screening and validation assay cascade, which led to the identification of the IMTs, have previously been published<sup>18</sup> and are described in detail in Extended Data Fig. 1a. In brief, a diverse set of 430,000 small chemical compounds was screened for inhibitory effects on the mitochondrial transcription machinery, using a patented (PCT/EP2016/062198) homogenous time-resolved fluorescence (HTRF)-based in vitro method to monitor product formation. The threshold for hit selection was set stringently to 30% residual activity, relative to the control (100% DMSO). After filtering out substances that displayed autofluorescence or fluorescence-quenching properties in the excitation or emission wavelength of the assay, 580 primary hits were selected for further analysis, corresponding to a hit rate of 0.13%. Dose-dependent activity was assessed in screening assay format, using serial compound dilutions. Substances displaying half-maximal inhibitory concentration ( $IC_{50}$ ) values lower than 10  $\mu$ M were subjected to structural clustering and filtering, followed by secondary assays to assess target engagement, selectivity and cellular toxicity. Finally, confirmed hit compounds were validated for their cellular activity using a quantitative PCR with reverse transcription (qRT-PCR) assay to measure transcription of the same mitochondrial transcript, which had been used in the high-throughput screening assay (mt-7S), in relation to nuclear-encoded POLRMT and a housekeeping gene in HeLa cells. Analysis yielded a group of 55 validated inhibitors, which were active in biochemical and cellular assays and were selective against POLRMT. Amongst these compounds, the IMT compounds described in this Article were selected for further medicinal chemistry development. Details on the synthesis of the IMTs can be found in Supplementary Methods. IMT1 (LDC195943) and IMT1B (LDC203974) dissolved in 100% DMSO were stored for up to three months at room temperature in the dark. For screening of IMT-resistant clones, the screening compound IMT (D060-0044, ChemDiv) was used. Con IMT (SC-6238532; ChemBridge) was used as a control compound. Cells were treated with 0.05% DMSO as a control.

### Differential scanning fluorimetry

The fluorescent dye Sypro Orange (Thermo Fisher Scientific;  $\lambda_{ex} = 490$  nm,  $\lambda_{em} = 570$  nm) was used to monitor the temperature-induced unfolding of apo- and inhibitor-bound human and mouse POLRMT. The assay was set up essentially as previously described<sup>31</sup>, with 0–10  $\mu$ M IMT1B and 1.6  $\mu$ M human POLRMT.

### Microscale thermophoresis

The effect of inhibitors on the binding affinity of human POLRMT to a DNA–RNA template was analysed using microscale thermophoresis (MST). A 28-mer 5' Alexa488-labelled non-template DNA oligonucleotide (5'-CATGGGTAATTATTATTCGCCAGACG-3') was annealed to its complementary template strand (5'-CG TCTGGCGTGC CGCCGCTACCCCAGT-3') and a 14-mer RNA oligonucleotide (5'-AGUCUGCGCGC-3') in a 1:1 molar ratio. Twelve 2-fold dilutions of POLRMT (0.45–1,000 nM) were made in MST buffer (25 mM Tris-HCl pH 8.0, 0.1 M NaCl, 10 mM MgCl<sub>2</sub>, 0.5 mM ATP, 10% (w/v) glycerol, 1 mM DTT and 0.05% (v/v) Tween-20). Dilutions were incubated with 15 nM DNA–RNA template and 0–10  $\mu$ M IMT1B for 10 min at 24 °C. Samples were analysed in triplicate using a Monolith NT.115 instrument (NanoTemper Technologies) with standard capillaries and 40% LED and MST power for 30 s at 24 °C. Combined thermophoresis

and temperature jump data were baseline-corrected and used to calculate  $K_d$ , bound state and unbound state in the NanoTemper analysis software.

### Protein expression and purification

Human and mouse POLRMT, mitochondrial transcription factor A (TFAM), mitochondrial transcription factor B2 (TFB2M) and TEFM were cloned and expressed as 6×His-tagged fusion proteins in *Spodoptera frugiperda* (Sf9) cells as previously described<sup>4,32</sup>. POLRMT point mutations (L816Q and A821V) were generated using a QuikChange XL site-directed mutagenesis kit (Agilent) and were expressed and purified as for wild-type POLRMT. For the in vitro transcription assay comparing IMT inhibition of POLRMT and RNA polymerase II, a variant of human POLRMT lacking the first 119 residues was purified as previously described<sup>33</sup>. *Sus scrofa* RNA polymerase II was isolated from thymus as previously described<sup>34</sup>.

### In vitro transcription assays

The effect of inhibitors on mitochondrial transcription was probed using an in vitro transcription assay on linear and supercoiled templates containing the mitochondrial LSP. Transcription reactions (25  $\mu$ l) were set up as previously described<sup>4</sup> in the presence of 0–10  $\mu$ M IMT1B, 500 fmol POLRMT, 1.5 pmol TFB2M, 2.5 pmol TFAM and 500 fmol TEFM. Transcription products were purified by ethanol precipitation and analysed on 8% denaturing polyacrylamide gels as previously published<sup>4</sup>. Experiments with the mouse transcription system were performed and analysed in the same way.

The in vitro transcription assays comparing IMT inhibition of POLRMT and RNA polymerase II were performed as previously described<sup>35</sup>, with slight modifications. The sequence of the template DNA was 5'-GAAACCCAGCACCCAGCACCCAGCAGCAGCACCAGGCTGGCCTG GCGCCTCTCAAGGTCCA-3'; the sequence of the non-template DNA was 5'-biotin-TTTTTTGGGACCTTGAGAGCGGCCAGGCCAGCCTCGGTG CCTGCTGGGTGCTGGGTGCTGGGGTTTC-3'; and the sequence of the RNA was 5'-6-FAM-UUUUUUUCAGGCCAGCC (all purchased from IDT DNA Technologies). POLRMT or Pol II were first incubated with either 1% DMSO or IMT before addition of nucleic acids. Final reaction conditions were 75 nM POLRMT or Pol II, 50 nM RNA-template DNA, 50 nM non-template DNA, 10  $\mu$ M NTPs, 20 mM Na HEPES pH 7.5, 100 mM NaCl, 3 mM MgCl<sub>2</sub>, 4% (v/v) glycerol and 1 mM DTT in a reaction volume of 10  $\mu$ l. Transcription was carried out for 5 min at 30 °C, quenched by the addition of 10  $\mu$ l 2× stop buffer (6.4 M urea, 50 mM EDTA pH 8.0, 1× TBE buffer and the samples were treated with 4  $\mu$ g of proteinase K (New England BioLabs) before denaturing gel electrophoresis (8 M urea, 20% acrylamide:bis-acrylamide 19:1 and 1× TBE gel). Products were visualized using the 6-FAM label with a Typhoon 9500 FLA Imager (GE Healthcare Life Sciences).

For steady-state standing-start kinetic assays, a 14-mer RNA oligonucleotide (5'-AGUCUGCGCGC-3') was  $\gamma$ -<sup>32</sup>P-ATP end-labelled using T4 polynucleotide kinase (Thermo Fisher Scientific). End-labelled RNA oligonucleotides were annealed to a 28-mer non-template DNA oligonucleotide and its complementary template strand as described in 'Microscale thermophoresis' (Extended Data Fig. 1d). Reactions (25  $\mu$ l) were set up as previously described<sup>4</sup>, with the following changes: 67 nM template, 2.68 nM POLRMT and 0–500 nM ATP in the absence or presence of IMT1B. The reactions were incubated at 32 °C for 1 min to measure initial velocity ( $v_0$ ). Transcription products were purified, analysed on 10% denaturing polyacrylamide sequencing gels and quantified as previously published<sup>4</sup>. Data were fit to a Michaelis–Menten rectangular hyperbola using nonlinear least-squares methods in SigmaPlot v.11.0. Residual plots were used to assess the accuracy and quality of the fits (Extended Data Fig. 1f).

The template used for steady-state standing-start kinetic analysis was also used to investigate effects of IMT1B on other polymerases. Experiments with POLRMT and RPO41 were performed as previously

# Article

described<sup>4</sup>, with the following changes: 4 nM template, 180 nM POLRMT or RPO41 and 100 μM ATP were added in the absence or presence of IMT1B as indicated in Extended Data Fig. 3a. *Escherichia coli* RNA polymerase (Biolabs) and T7 RNA polymerase (Biolabs) transcription reactions were performed according to the manufacturer's instructions using 4 nM template and 100 μM ATP. Reverse transcriptase (Thermo Scientific RevertAid First Strand cDNA kit) reactions were performed according to the manufacturer's instructions using the control RNA provided as template. POLy activity was analysed using a 32-nt DNA oligonucleotide that had been annealed to an approximately 3-kb circular single-stranded DNA substrate, following a previously published protocol<sup>36</sup>. The chain terminator ddCTP (final concentration 100 μM) was used as a positive control.

## Protein purification for cryo-EM and structure determination

A construct representing the mature form of human POLRMT (lacking residues 1–43, mtRNAP(Δ43)) was generated from the previously described mtRNAP(Δ104) construct<sup>21</sup>. The protein was expressed and purified essentially as previously described<sup>21</sup>. In brief, BL21 (DE3) RIL cells (Agilent) were grown to an optical density at 600 nm of 0.6 units and expression was induced by addition of 0.15 mM IPTG and carried out at 16 °C for 18 h. POLRMT was purified by Ni-NTA affinity chromatography (Ni-NTA Agarose, Qiagen) followed by tag cleavage using TEV protease and heparin affinity chromatography (HiTrap HP 5 ml, GE Healthcare). Final purification was done by size-exclusion chromatography using a Superdex 200 Increase 10/300 column (GE Healthcare) equilibrated with a buffer containing 40 mM Tris/HCl pH 8.0, 300 mM NaCl, 20 mM MgCl<sub>2</sub>, 10 mM DTT and 5% glycerol. The protein was concentrated and stored at –80 °C.

To form a POLRMT–IMT1B complex, POLRMT was exchanged into a buffer containing 20 mM Tris/HCl pH 8.0, 300 mM NaCl, 5 mM MgCl<sub>2</sub>, 1 mM DTT and 50 μM IMT1B by repeated dilution followed by concentration in a 50-kDa cut-off concentrator (fivefold dilution, repeated three times). Grids were prepared using a Vitrobot (FEI) by adding 4 μl of approximately 4 μM POLRMT–IMT1B complex to glow-discharged UltrAuFoil 2/2 grids (Quantifoil) at 4 °C and 100% humidity. Grids were blotted for 6 s with a blot force of 5 and plunge-frozen in liquid ethane. Cryo-EM data were collected on a Titan Krios G2 (FEI) operated at 300 kV and equipped with a K3 direct electron detector (Gatan) and a BioQuantum energy filter (Gatan) set to a slit width of 20 eV. Non-super-resolution movies consisting of 40 frames were collected at a nominal magnification of 105,000× corresponding to a pixel size of 0.834 Å per pixel and with a total dose of 36.25 e<sup>−</sup> per Å (ref.<sup>5</sup>). Contrast-transfer function (CTF) estimation, motion correction and unsupervised particle picking and extraction was done using Warp (v.1.0.7)<sup>37</sup>. Two-dimensional classification was done using cryoSPARC (2.14.2)<sup>38</sup> and all subsequent processing steps were done using RELION (v.3.0.7)<sup>39</sup>.

Analysis of an initial dataset revealed that POLRMT adopts a preferred orientation in the vitrified ice, which resulted in a highly anisotropic three-dimensional reconstruction and limited interpretability. We attempted to overcome this problem using various approaches previously reported in the literature, including addition of detergent, addition of interacting proteins (TEFM) and the use of graphene oxide or continuous carbon support. However, none of these approaches led to a more favourable distribution of views. We therefore collected a dataset consisting of 2,077 micrographs at 40° stage tilt<sup>40</sup>. Following 2D classification and ab initio reference model generation in cryoSPARC, 3D classification using RELION yielded a particle subset with improved viewing distribution compared to the untilted data (Extended Data Fig. 5). This subset was subjected to global 3D refinement and subsequent further 3D classification, which yielded two classes of similar quality. Following CTF and beam tilt refinement as well as Bayesian polishing, particles were subjected to 3D autorefinement with a soft mask encompassing the entire particle, leading to a reconstruction

at an average resolution of 3.5 Å after post-processing (Fourier shell correlation threshold = 0.143). This reconstruction still showed anisotropy and its quality varied in different parts of the map. However, the region corresponding to the core of the enzyme, and in particular the region where IMT1B is bound, allowed for unambiguous assignment of side-chain locations.

To build the POLRMT structure, the protein part of the human mitochondrial transcription elongation complex (PDB 4BOC)<sup>6</sup> was first rigid-body fit into the cryo-EM map. The PPR domain (residues 221–365) was rigid-body fit separately and not further modified manually, as this region of the map was of lower quality than the polymerase core. The rest of the model was manually fitted in real space in Coot (v.0.9.)<sup>41</sup>. The most prominent difference between the initial model and the cryo-EM reconstruction was observed for a loop in the palm domain (residues 811–819), which could be rebuilt unambiguously. After completion of the POLRMT model, an unaccounted bilobal elongated density remained between the thumb and the palm domain, where IMT1B was expected to bind on the basis of our mutational data. Coordinates and restraints for IMT1B were created in phenix.elbow (v.1.18.)<sup>42</sup> and positioned in the density. It is noteworthy that at the resolution obtained and with the residual anisotropy in the cryo-EM reconstruction, it is not possible to unambiguously determine the orientation of IMT1B on the basis of the density alone. However, on the basis of chemical considerations, we reason that IMT1B is likely to be orientated such that its halogenated aromatic ring is buried in the hydrophobic pocket between the thumb and palm domains, and to have its polar carboxy group facing outwards towards the solvent (Extended Data Fig. 5d). Overall, this orientation is in good agreement with the density and chemical surroundings and therefore seems the most likely. The structure was refined using phenix.real\_space\_refine (v.1.18.)<sup>42</sup> with secondary structure restraints and the human mitochondrial transcription elongation complex (PDB 4BOC)<sup>6</sup> as a reference model restraint. The final structure shows good stereochemistry, with 95.99, 3.23 and 0.78% of residues in favoured, preferred and disallowed regions, respectively (Supplementary Table 1).

## Cell lines and cell culture

HeLa cells (ATCC CCL-2) and A2780 cells (ECACC 93112519) were cultured in Dulbecco's modified Eagle medium (DMEM) with 1 g l<sup>−1</sup> glucose (Thermo Fisher Scientific), supplemented with 10% (v/v) fetal bovine serum (FBS) (Thermo Fisher Scientific) and antibiotics (penicillin–streptomycin) (Thermo Fisher Scientific). A complete overview of all 89 cell lines used in the IMT1 cell proliferation panel (as discussed in 'Cell viability assays and ROS measurement') and their sources is given in Supplementary Table 2. Cell lines were authenticated as indicated by the manufacturer by short-tandem repeat analysis and compared to the International Cell Line Authentication Committee (ICLAC) register of misidentified cell lines (version 10). No misidentified cell line was included here. To determine the effects of IMT treatment on primary human cells, human PBMCs (buffy coats from DRK West Blutspendedienst Hagen) and five-donor mixed-gender pooled human hepatocytes (BioreclamationIVT) were used. To generate biological replicates for reactive oxygen species (ROS) measurements, proteomic and metabolomic analyses, single cells were sorted from a suspension of A2780 cells into a 96-well cell culture dish. Five different clones were subsequently grown to confluence and used for the indicated analyses. Cells were kept at 37 °C and 5% CO<sub>2</sub> in a humidified atmosphere in a cell culture incubator and passaged twice a week. The number of viable cells was determined by trypan blue exclusion using an automated cell counter (Vi-Cell XR Cell viability analyser, Beckman Coulter).

Short interfering (si)RNA transfection of HeLa cells was performed as previously described<sup>1</sup>, using Mission esiRNA pools (Sigma) against either EGFP (EHUEGFP) or human POLRMT (EHU012581). The target cDNA sequences used to generate Mission esiRNA pools are given in Supplementary Table 3. After the final round of transfection, HeLa cells

were seeded at  $0.5 \times 10^6$  cells per well in 6-well dishes. Cell number was assessed after four days using an automated cell counter.

### Gene editing and genotyping by Sanger sequencing

Specific POLRMT mutations were engineered in wild-type A2780 cells using the CRISPR–Cas9 technology as previously described<sup>19</sup>.

### Ethylnitrosourea treatment and drug selection

For chemical mutagenesis A2780 cells were mutagenized with 0.1 mg/ml ethylnitrosourea, as previously described<sup>19</sup>. Drug selection was performed for 21 days, starting 24 h after mutagenesis using 10  $\mu$ M of precursor IMT.

### DNA extraction, exome sequencing and analysis

DNA extraction from resistant colonies as well as the sequencing and analysis procedures have previously been described in detail<sup>19</sup>.

### Mouse lines and xenografts

For in organello translation experiments, wild-type male C57Bl/6N mice were used (age of 10–14 weeks). Mice were housed in standard individually ventilated cages in a 12 h light/dark cycle in controlled environmental conditions ( $21 \pm 2^\circ\text{C}$ , 50% to 60% relative humidity). Mice were fed a normal chow diet and water ad libitum.

A2780 xenograft models were conducted at EPO Berlin-Buch using female *NMRI<sup>nu/nu</sup>* mice obtained from Janvier Labs. Mice were 7–9 weeks of age on the day of arrival. Mice were housed in standard individually ventilated cages (maximum five mice per cage) in a 12 h light/dark cycle in controlled environmental conditions ( $22 \pm 2^\circ\text{C}$ , 50% to 60% relative humidity). Mice were fed a normal chow diet and water ad libitum. Tumour-bearing mice were stratified into groups of eight mice according to the tumour volume to achieve a similar distribution of individual tumour volumes in each group. Distribution of individual mice into groups was then randomized.

The DLD-1 xenograft model was conducted at Crown Bioscience, using female BALB/c nude mice (7–9 weeks of age), supplied by Beijing HFK Bioscience. Mice were housed in standard individually ventilated cages (maximum four mice per cage) in a 12 h light/dark cycle in controlled environmental conditions ( $22.3 \pm 2^\circ\text{C}$ , 44–58% relative humidity). Mice were fed a normal chow diet and water ad libitum. Group assignment was based on a stratified random sampling procedure. All experimental procedures were approved by and conducted in accordance with the regulations of the local Animal Welfare Authorities. Human ovary carcinoma A2780 (ECACC 93112519) ( $5 \times 10^7$  cells in 100  $\mu$ l of PBS and Matrigel) or DLD-1 colon carcinoma cells ( $5 \times 10^6$  cells in 100  $\mu$ l of PBS and Matrigel), isolated during exponential growth phase from *in vitro* cell culture, were transplanted subcutaneously into each female nude mice at day 0. Mice were stratified ( $n = 8$  per group each) when the mean tumour volume had reached approximately  $0.1 \text{ cm}^3$ . Mice were orally treated with either vehicle or 100 mg per kg body weight IMT1B. IMT1B was administered using 25% PEG400 in 30% aqueous hydroxypropyl- $\beta$ -cyclodextrin as vehicle. Measurement of body weight and tumour volume was performed three times per week. For A2780 xenografts, individual mice were killed if tumour volumes progressed to  $>1.5 \text{ cm}^3$ ; if the mean tumour volume of a group was  $>1 \text{ cm}^3$ ; or if ulceration was observed. For DLD-1 xenografts, individual mice were killed if tumour volumes progressed to  $>3 \text{ cm}^3$ ; if the mean tumour volume of a group was  $>2 \text{ cm}^3$ ; or if ulceration was observed. A gross autopsy was performed from all mice upon study termination and tissues samples were isolated.

### RNA isolation, cDNA synthesis and qRT–PCR

Total RNA was isolated from cultured cells or snap-frozen tissue samples using TRIzol Reagent (Thermo Fisher Scientific) following the manufacturer's instructions and subsequently DNase-treated (TURBO DNA-free kit, Thermo Fisher Scientific). Alternatively, total RNA was

isolated using the Direct-zol RNA Miniprep Kit (ZymoResearch) including the DNase digestion step. The purity and quantity of RNA were evaluated with the NanoDrop 2000 (Thermo Scientific). cDNA was synthesized using the High-Capacity RNA-to-cDNA Kit (Applied Biosystems). qRT–PCR was carried out using the Taqman 2 $\times$  Universal PCR mastermix, No Amperase UNG (Applied Biosystems) and commercially available Taqman assay probes for human and mouse mitochondrial transcripts (Supplementary Table 4). Transcript quantities were normalized to  $\beta$ -actin or  $\beta$ -2-microglobuline, which were used as reference gene transcripts.

### DNA isolation and determination of mtDNA levels by qPCR

Total DNA was extracted and purified using the Dneasy blood and tissue kit (Qiagen) or the Puregene Core A Kit (Qiagen) following the manufacturer's instructions including RNase treatment. The purity and quantity of DNA were evaluated with the NanoDrop 2000 (Thermo Scientific) and 5–10 ng  $\mu\text{l}^{-1}$  DNA were analysed by qPCR. qPCR was carried out using the Taqman 2 $\times$  Universal PCR mastermix, No Amperase UNG (Applied Biosystems) and commercially available Taqman assay probes for human (*COX1* (also known as *MT-CO1*) and mouse (*Cox1* (also known as *mt-Co1*)) mitochondrial and nuclear DNA (18S).

### Western blotting

For cell culture experiments, cell pellets were lysed in RIPA buffer (Pierce) containing a protease inhibitor cocktail (Roche) and protein quantification was assessed using the bicinchoninic acid assay (Thermo Fisher Scientific) or the reducing agent and detergent compatible (RCDC) assay (Biorad). For xenograft analysis, proteins were extracted from grinded tissue powder using 2 $\times$  SDS-sample buffer (100 mM Tris pH 6.8, 4% SDS, 20% glycerol and 200 mM DTT). Protein concentration was determined using the RCDC assay (Biorad). Proteins were resolved by SDS-PAGE using commercially available 10% or 4–12% NuPAGE Bis-Tris gels and MOPS buffer (Invitrogen) including protein standards (Spectra Multicolor Broad Range or Magic Mark XP Western, Thermo Fisher Scientific) and transferred on nitrocellulose membranes. Immunodetection was performed by enhanced chemiluminescence (GE Healthcare) using either photo film or the Fujifilm LAS 400 imaging system (Fujifilm). The following antibodies were used: mouse monoclonal anti-COX1 (MT-CO1, ab14705, Abcam, 1:2,000), mouse monoclonal anti-actin (ab3280, Abcam, 1:2,000), total OXPHOS Rodent WB antibody cocktail (ab110413, Abcam, 1:2,000), rabbit anti-phospho S6 ribosomal protein (no. 4856, Cell Signaling, 1:1,000), rabbit anti-S6 ribosomal protein (no. 2217, Cell Signaling, 1:2,000), rabbit anti-phospho AMPK (no. 2535, Cell Signaling, 1:1,000), rabbit anti-AMPK (no. 2532, Cell Signaling, 1:1,000), rabbit anti-LRPPRC (self-made<sup>43</sup>, RRID:AB\_2716302, 1:1,000), rabbit anti-vinculin (ab129002, Abcam, 1:2,000), rabbit anti-tubulin (no. 2125, Cell Signaling, 1:2,000), mouse anti-tubulin (T9026, Sigma, 1:2,000), mouse anti-PCNA (ab29, Abcam, 1:1,000), cleaved PARP (from Cell Cycle and Apoptosis cocktail, ab139417, Abcam, 1:250), rabbit anti-POLRMT (sc-67350, Santa Cruz, 1:600), rabbit anti-HSP60 (no. 4870, Cell Signaling, 1:1,000), sheep anti-mouse IgG (NXA931V, GE Healthcare, standard: 1:3,000) and donkey anti-rabbit (NA9340V, GE Healthcare, standard: 1:3,000).

### In organello translation

In organello translation experiments were carried out as previously described<sup>44</sup>. Translation buffer used for washing and S-35 labelling was supplemented with either DMSO or 5  $\mu$ M IMT1B.

### Intact cell respiration

Intact cell respiration was assessed in standard DMEM culture medium (low glucose 5.5 mM). Basal oxygen consumption was determined in DMEM in the presence of glutamate and pyruvate (4 and 1 mM, respectively). After inhibition of the mitochondrial phosphorylation by adding

# Article

oligomycin (1 µM) to determine the oxidative leak, the mitochondrial electron transport chain was stimulated maximally by the addition of the uncoupler carbonyl cyanide *m*-chlorophenyl (CCCP) (2 µM). Finally, extra-mitochondrial respiration was determined after the addition of rotenone (0.5 µM) and antimycin A (2.5 µM). For the determination of the basal respiration, the oxidative leak and the maximal respiration, extra-mitochondrial respiration was subtracted.

## Cell viability assays and ROS measurement

Relative cell viability of wild-type and mutant A2780 cell lines was assessed using the XTT cell proliferation Kit II (Roche Diagnostics) according to the manufacturer's instructions. Drug treatments were performed for 144 h, starting 24 h after cell seeding. XTT turnover was normalized to corresponding untreated control cells. Cell viability in human PBMCs and primary human hepatocytes was analysed by measuring the intracellular ATP content using the CellTiter-Glo Luminescent Cell Viability Assay (Promega) in accordance with the manufacturer's guidelines. A panel of 89 cancer cell lines of different tissue origin (Supplementary Table 2) was profiled using IMT1 in dose-dependent fashion (30 µM to 0.3 nM) at Oncolead. Cells were cultivated in high glucose medium (25 mM). The compound was applied in a cell culture protocol allowing for prolonged incubation times ( $\geq$ 168 h). Compounds were added 24 h after cell seeding and a first absorbance measurement. Cell viability was measured using the SRB assay. Measurements at 72 or 168 h after compound addition were used to determine IC<sub>50</sub> values. Indeed, measurements after 72 h revealed only minor effects of the IMT1, whereas longer incubation times resulted in much more potent inhibition of cell proliferation under these conditions.

For detection of cellular ROS levels, 5 different A2780 clones (10,000 cells per well) were seeded into black 96-well cell culture dishes (Greiner bio-one) and treated with either DMSO or 5 µM IMT1 24 h after seeding. Cells were incubated in the presence of either DMSO or IMT1 for 0–96 h and ROS levels were analysed using the Cellular ROS Assay Kit (Orange) (Abcam) according to the manufacturer's instructions using a TECAN fluorimeter.

## Quantitative proteomics

For quantitative proteomics, cells derived from 5 different A2780 clones were seeded into 12-well cell culture dishes ( $0.5 \times 10^6$  cells per well). Twenty-four h after seeding, cells were treated with DMSO or 5 µM IMT1 for the indicated time points (0–96 h). All samples corresponding to one time point were collected from the same cell culture dish by trypsinization. Sample preparation was performed as previously described<sup>45</sup>, with slight modifications: tryptic peptides were eluted from STAGE tips with 40% acetonitrile (ACN) and 0.1% formic acid (FA). Four micrograms of desalted peptides were labelled with tandem mass tags (TMT10plex, cat. no. 90110, Thermo Fisher Scientific) using a 1:20 ratio of peptides to TMT reagent. All ten samples per time point were labelled in one TMT batch. TMT labelling was carried out according to manufacturer's instruction with the following changes: 0.8 mg of TMT reagent was resuspended with 70 µl of anhydrous ACN, dried peptides were reconstituted in 9 µl 0.1 M TEAB to which 7 µl TMT reagent in ACN was added to a final ACN concentration of 43.75%, and after 60 min of incubation the reaction was quenched with 2 µl 5% hydroxy-lamine. Labelled peptides were pooled, dried, resuspended in 200 µl 0.1% FA, split into two samples and desalted using home-made C18 STAGE tips<sup>46</sup>. One of the two halves was fractionated on a 1 × 150-mm ACQUITY column, packed with 130 Å, 1.7-µm C18 particles (Waters cat. no. SKU: 186006935), using an Ultimate 3000 UHPLC (Thermo Fisher Scientific). Peptides were separated at a flow of 30 µl min<sup>-1</sup> with a 96-min segmented gradient from 1% to 50% buffer B for 85 min and from 50% to 95% buffer B for 3 min, followed by 8 min of 95% buffer B; buffer A was 5% ACN and 10 mM ammonium bicarbonate (ABC), and buffer B was 80% ACN and 10 mM ABC. Fractions were collected every three minutes, and fractions were pooled in two passed (1 + 17, 2 + 18 and so

on) and dried in a vacuum centrifuge (Eppendorf). Dried fractions were resuspended in 0.1% FA separated on a 50-cm, 75-µm Acclaim PepMap column (Thermo Fisher Scientific, cat. no. 164942) and analysed on a Orbitrap Lumos Tribrid mass spectrometer (Thermo Fisher Scientific) equipped with a FAIMS device (Thermo Fisher Scientific) that was operated in two compensation voltages (-50 V and -70 V). Alternatively, peptides were separated on a 25-cm, 75-µm PicoFrit column (New Objective) packed with 1.9-µm ReproSil-Pur medium (Dr. Maisch) and analysed on an Orbitrap Fusion Tribrid mass spectrometer (Thermo Fisher Scientific). Synchronous precursor selection-based MS3 was used for TMT reporter ion signal measurements. Peptide separations were performed on an EASY-nLC1200 using a 90-min linear gradient from 6% to 31% buffer; buffer A was 0.1% FA, and buffer B was 0.1% FA and 80% ACN. The analytical column was operated at 50 °C. Raw files were split based on the FAIMS compensation voltage using FreeStyle (v.1.6, Thermo Fisher Scientific).

Proteomics data were analysed using MaxQuant<sup>47</sup> (v.1.6.10.43). Raw proteomics data were searched against the human proteome database from UniProt, downloaded in September 2018. The isotope purity correction factors, provided by the manufacturer, were included in the analysis. Differential expression analysis was performed using limma<sup>48</sup> in R (v.1.1.383).<sup>49</sup> Two samples of time point 0 h IMT1 treatment were excluded from the analysis owing to a low TMT reporter distribution. An extra variable that accounts for an experimental batch effect was used in the analysis. The raw data, database search results and the data analysis workflow and results have been deposited in the ProteomeXchange Consortium via the PRIDE partner repository<sup>50</sup>, with the dataset identifier PXD018426.

## Metabolite extraction for liquid chromatography mass spectrometry

For metabolomics, cells derived from 5 different A2780 clones were seeded into 6-well cell culture dishes ( $1 \times 10^6$  cells per well). Twenty-four h after seeding, cells were treated with DMSO or 5 µM IMT1 for the indicated time points (48–216 h). After carefully removing the growth medium, cells were washed twice with 1 ml of ammonium carbonate buffer (75 mM, pH 7.4) warmed to 37 °C. After the washing step, metabolites were extracted by 2 consecutive 20-min incubation steps with each 400 µl of pre-cooled (-20 °C) extraction buffer (40/40/20 (v/v/v) ACN/methanol/water, containing 10 ng ml<sup>-1</sup><sup>13</sup>C<sub>10</sub>ATP, citric acid d4 (Sigma 710695, 485438), as well as 2.5 nM uniformly <sup>13</sup>C<sup>15</sup>N-labelled amino acids (Cambridge Isotope Laboratories, MSK-A2-1.2). The consecutive extracts were pooled and the centrifuged at 21,000g at 4 °C for 10 min. Supernatants were transferred to fresh tubes and dried down using a speed vac concentrator (Eppendorf). Samples were re-suspended in 100 µl liquid chromatography mass spectrometry (LC-MS)-grade H<sub>2</sub>O (Thermo Fisher Scientific) of which 80 µl was used to perform anion-exchange chromatography for the analysis of glycolysis, TCA, nucleotide and deoxy nucleotide metabolites, and 20 µl was used for the analysis of amine-containing metabolites using a benzoyl chloride derivatization method.

## LC-MS analysis of amine-containing metabolites

A benzoyl chloride derivatization method was used for amino acid analysis, as previously described<sup>51</sup>. One µl of derivatized samples was separated using a Vanquish UHPLC (Thermo Fisher Scientific) connected to a Q-Exactive HF (Thermo Fisher Scientific). The mass spectrometer was operated in positive ionization mode monitoring the mass range *m/z* 50–750. The heated electrospray ionization source settings of the mass spectrometer were: spray voltage 3.5 kV, capillary temperature 250 °C, sheath gas flow 60 AU and aux gas flow 20 AU at a temperature of 250 °C. The S-lens was set to a value of 60 AU.

Data analysis was performed using the TraceFinder software (v.4.1, Thermo Fisher Scientific). The identity of each compound was validated by authentic reference compounds, which were analysed

independently. Peak areas were analysed by using extracted ion chromatogram of compound-specific  $[M+nBz+H]^+$ , in which  $n$  corresponds to the number of amine moieties that can be derivatized with a benzoyl chloride (Bz). Extracted ion chromatogram peaks were extracted with a mass accuracy (<5 ppm) and a retention time tolerance of 0.05 min.

For peak area normalization, we corrected each peak for the intensities of the appropriate internal standard that were spiked into the extraction buffer. Additionally, we normalized for the sample amount equivalent by correcting the obtained peak areas by the average ion count (AIC) of each sample. The AIC was derived from the untargeted extraction and alignment of 5,296 peaks from each sample using the Progenesis QI software (v.2.3, Nonlinear). Each metabolic peak area in the targeted analysis was divided by the scaled AIC factor (AIC divided by  $10^5$ ), leading to a graded correction by the metabolite intensity within each sample.

### Anion-exchange chromatography mass spectrometry of the analysis of TCA cycle and glycolysis metabolites

For the chromatographic separation of anions, we used a previously published method<sup>52</sup>. The eluting metabolites were detected in negative ion mode using electrospray ionization multi-reaction monitoring (ESI MRM) on a Xevo TQ (Waters) triple quadrupole mass spectrometer applying the following settings: capillary voltage 2.5 kV, desolvation temperature 550 °C, desolvation gas flow 800 l h<sup>-1</sup>, collision cell gas flow 0.15 ml min<sup>-1</sup>. All peaks were validated using two MRM transitions: one for quantification of the compound and the other for qualifying the identity of the compound. The settings for the MRM transitions are given in the Supplementary Table 5.

Data analysis and peak integration was performed using the Target-Lynx Software (4.1 SCN 950, Waters).

For peak area normalization, we corrected each peak for the intensities of the appropriate internal standard that were spiked into the extraction buffer. Additionally, we normalized for the sample amount equivalent by correcting the obtained peak areas by the average ion count (AIC) obtained from the untargeted extraction and alignment of 5,296 peaks from the LC–MS analysis of amine-containing compounds, using the Progenesis QI software (v.2.3, Nonlinear). Each metabolic peak area in the targeted analysis was divided by the scaled AIC factor (AIC divided by  $10^5$ ), leading to a graded correction by the metabolite intensity within each sample.

### Toxicity panels

Toxicity panels, blood parameters and pharmacokinetic analyses were carried out at Synovo. Mice (4 per cage) were housed in standard individually ventilated cages in a 12 h light/dark cycle in controlled environmental conditions (22 ± 1 °C, 55–65% relative humidity). Mice were fed a normal chow diet and water ad libitum. All experimental procedures were approved by and conducted in accordance with the regulations of the local Animal Welfare Authorities (Tübingen Regional Council).

For toxicity and blood parameters, female NMRI mice obtained from Janvier Labs were used. Before allocation, mice were weighed and groups were assigned according to a randomized block design such that mean starting weight was similar in all groups. Mice received either vehicle (25% PEG400 in 30% aqueous hydroxypropyl-β-cyclodextrin) or 100 mg per kg body weight IMT1B once daily for four weeks followed by a wash-out period. Body weight was measured once daily. Blood samples were taken for analysis at day 0 and day 28.

To establish a suitable dosing regimen for an in vivo efficacy study, the pharmacokinetic profiles of the test compounds after administration of single doses of 1 mg per kg intravenously and 10 mg per kg orally to male CD1 mice were determined. Plasma samples were obtained over a 24-h interval and test compound concentrations were analysed by LC–MS. To this end, test compounds were extracted from plasma by protein precipitation using ACN. Samples were analysed by

liquid chromatography–tandem mass spectrometry using a Prominence UFLC system (Shimadzu) coupled to a Qtrap 5500 instrument (ABSciex). Test compounds were separated on a C18 column with an ACN and water mixture containing 0.1% formic acid as solvent. Chromatographic conditions and mass spectrometer parameters were optimized for each test compound before sample analysis. Concentrations of each test compound were calculated by means of a standard curve. Pharmacokinetic parameters were calculated by non-compartmental analysis using PKSolver Plug-in for Microsoft Excel (v.2.0)

### Statistical analysis

Data are given as mean ± s.e.m. or mean ± s.d., as indicated in the figure legends. Details of the number of biological replicates and independent experiments are given in the figure legends. Statistical analysis was performed using GraphPad Prism (v.8.0, GraphPad Software) and the statistical test used and *P* values are given in the figures and/or figure legends. Exact *P* values are given in the respective Source Data files.

### Reporting summary

Further information on research design is available in the Nature Research Reporting Summary linked to this paper.

### Data availability

All relevant data generated and analysed in this study are included in the Article. Uncropped gels are provided in Supplementary Fig. 1. Publicly available datasets used in this study are the human proteome database (UP000005640, UniProt) and POLRMT structures (PDB codes SOLA and 4BOC). Further information and requests for unique reagents should be directed to the corresponding authors. Proteomics data and R scripts for analysis have been deposited in PRIDE with the dataset identifier PXD018426. The electron microscopy maps have been deposited with the Electron Microscopy Data Bank (accession code EMD-11679) and the structural model of POLRMT bound to IMT1B has been deposited in the PDB (accession code 7A8P). Source data are provided with this paper.

31. Peter, B. et al. Defective mitochondrial protease LonP1 can cause classical mitochondrial disease. *Hum. Mol. Genet.* **27**, 1743–1753 (2018).
32. Falkenberg, M. et al. Mitochondrial transcription factors B1 and B2 activate transcription of human mtDNA. *Nat. Genet.* **31**, 289–294 (2002).
33. Morozov, Y. I. et al. A novel intermediate in transcription initiation by human mitochondrial RNA polymerase. *Nucleic Acids Res.* **42**, 3884–3893 (2014).
34. Vos, S. M., Farnung, L., Urlaub, H. & Cramer, P. Structure of paused transcription complex Pol II-DSIF-NELF. *Nature* **560**, 601–606 (2018).
35. Vos, S. M., Farnung, L., Linden, A., Urlaub, H. & Cramer, P. Structure of complete Pol II-DSIF-PAF-SPT6 transcription complex reveals RTF1 allosteric activation. *Nat. Struct. Mol. Biol.* **27**, 668–677 (2020).
36. Macao, B. et al. The exonuclease activity of DNA polymerase γ is required for ligation during mitochondrial DNA replication. *Nat. Commun.* **6**, 7303 (2015).
37. Tegunov, D. & Cramer, P. Real-time cryo-electron microscopy data preprocessing with Warp. *Nat. Methods* **16**, 1146–1152 (2019).
38. Punjani, A., Rubinstein, J. L., Fleet, D. J. & Brubaker, M. A. cryoSPARC: algorithms for rapid unsupervised cryo-EM structure determination. *Nat. Methods* **14**, 290–296 (2017).
39. Scheres, S. H. RELION: implementation of a Bayesian approach to cryo-EM structure determination. *J. Struct. Biol.* **180**, 519–530 (2012).
40. Tan, Y. Z. et al. Addressing preferred specimen orientation in single-particle cryo-EM through tilting. *Nat. Methods* **14**, 793–796 (2017).
41. Emsley, P., Lohkamp, B., Scott, W. G. & Cowtan, K. Features and development of Coot. *Acta Crystallogr. D* **66**, 486–501 (2010).
42. Adams, P. D. et al. PHENIX: a comprehensive Python-based system for macromolecular structure solution. *Acta Crystallogr. D* **66**, 213–221 (2010).
43. Ruzzene, B. et al. LRPPRC is necessary for polyadenylation and coordination of translation of mitochondrial mRNAs. *EMBO J.* **31**, 443–456 (2012).
44. Kauppinen, J. H. K. et al. Base-excision repair deficiency alone or combined with increased oxidative stress does not increase mtDNA point mutations in mice. *Nucleic Acids Res.* **46**, 6642–6669 (2018).
45. Busch, J. D. et al. MitoRibo-tag mice provide a tool for in vivo studies of mitoribosome composition. *Cell Rep.* **29**, 1728–1738 (2019).
46. Rappasilber, J., Ishihama, Y. & Mann, M. Stop and go extraction tips for matrix-assisted laser desorption/ionization, nanoelectrospray, and LC/MS sample pretreatment in proteomics. *Anal. Chem.* **75**, 663–670 (2003).

# Article

47. Cox, J. & Mann, M. MaxQuant enables high peptide identification rates, individualized p.p.b.-range mass accuracies and proteome-wide protein quantification. *Nat. Biotechnol.* **26**, 1367–1372 (2008).
48. Ritchie, M. E. et al. limma powers differential expression analyses for RNA-sequencing and microarray studies. *Nucleic Acids Res.* **43**, e47 (2015).
49. R Development Core Team. R: A Language and Environment for Statistical Computing (R Foundation for Statistical Computing, 2010).
50. Perez-Riverol, Y. et al. The PRIDE database and related tools and resources in 2019: improving support for quantification data. *Nucleic Acids Res.* **47**, D442–D450 (2019).
51. Wong, J. M. et al. Benzoyl chloride derivatization with liquid chromatography-mass spectrometry for targeted metabolomics of neurochemicals in biological samples. *J. Chromatogr. A* **1446**, 78–90 (2016).
52. Schwaiger, M. et al. Anion-exchange chromatography coupled to high-resolution mass spectrometry: a powerful tool for merging targeted and non-targeted metabolomics. *Anal. Chem.* **89**, 7667–7674 (2017).

**Acknowledgements** This work was supported by the Max Planck Society, the Swedish Research Council (2015-00418 to N.-G.L., 2013-3621 to M.F., 2012-2583 to C.M.G.), Swedish Cancer Foundation (to M.F., C.M.G. and N.-G.L.), the Knut and Alice Wallenberg foundation (to M.F., C.M.G. and N.-G.L.), the Deutsche Forschungsgemeinschaft (SFB1218/A06 to N.-G.L.), European Research Council (Advanced Grant 2016-741366 to N.-G.L.) and grants from the Swedish state under the agreement between the Swedish government and the county councils, the ALF agreement to M.F. (ALFGBG-727491), C.M.G. (ALFGBG-728151) and N.-G.L. (SLL2018.0471). P.C. was supported by the Deutsche Forschungsgemeinschaft (SFB860, SPP1935), the European Research Council (advanced investigator grant TRANSGEULON, grant agreement no. 693023), the Volkswagen Foundation and Germany's Excellence Strategy (EXC 2067/1-390729940). H.S.H. was supported by the Deutsche Forschungsgemeinschaft (FOR2848). We thank N. Hochhard and S. Miethe for technical assistance; M. del Pilar Miranda for assistance; T. Colby, A. Taha, Y. Hinze, S. Perin and C. Edlich-Muth for support; I. Ivanov at Oncolead for providing cell panel data; C. Dienemann for assistance with cryo-EM data collection and processing; and Y. Chen for providing purified RNA polymerase II.

**Author contributions** M.F., C.M.G. and N.-G.L. conceptualized the original IMT idea. M.F., C.M.G., N.-G.L., B.K., N.A.B. and B.P. conceptualized research goals and experiments. N.A.B. and B.P. planned, performed and analysed the majority of the experiments. N.A.B. conducted

and analysed qPCR and western blotting experiments in tissue culture (IMT1, IMT1B and con IMT) and xenografts, performed and analysed siRNA transfection experiments, cell proliferation assays, ROS measurement, metabolomics, quantitative proteomics and in organello translation assays. B.P. performed and analysed differential scanning fluorimetry, microscale thermophoresis analysis and in vitro transcription assays (IMT1, IMT1B and con IMT) and expressed mutant POLRMT constructs. H.S.H. designed and carried out cryo-EM experiments and RNA Pol II primer extension assays. A.F. planned, performed and analysed qPCR, western blotting and respiration measurements using IMT1. T.B. designed the HTRF-based POLRMT detection method and analysed experiments in the course of IMT development. A.C. and P.H. planned, performed and analysed cell proliferation assays. M.H. planned, performed and analysed the forward genetic screens and generated A2780 mutant cell lines. A.U. designed and analysed toxicology, pharmacology and efficacy data. R.L. designed IMT compounds and synthesis routes, analysed data and devised strategies to elaborate the structure–activity relationship of inhibitors. I.A. and X.L. performed, analysed and interpreted quantitative proteomics data. P.G. performed, analysed and interpreted metabolomics data. U.K. carried out structural modelling of human POLRMT, docking of compounds and aided in cluster analysis of inhibitors. S.M. and J.B. designed and carried out qPCR and western blot experiments in the course of IMT development. M.S.D. planned and interpreted the forward genetic screens. P.N. aided in compound and synthesis design. P.C. designed and supervised cryo-EM experiments and RNA Pol II primer extension assays. M.F. planned, performed and analysed in vitro assays on RPO41, T7 RNA Pol, *E. coli* RNA Pol, RevertAid reverse transcriptase and POLG. N.A.B., B.P., C.M.G. and N.-G.L. wrote the manuscript, with input from all authors.

**Competing interests** The IMT compound intellectual property is published as WO 2019/057821 and has been licensed by the Max Planck Society and the Lead Discovery Center GmbH.

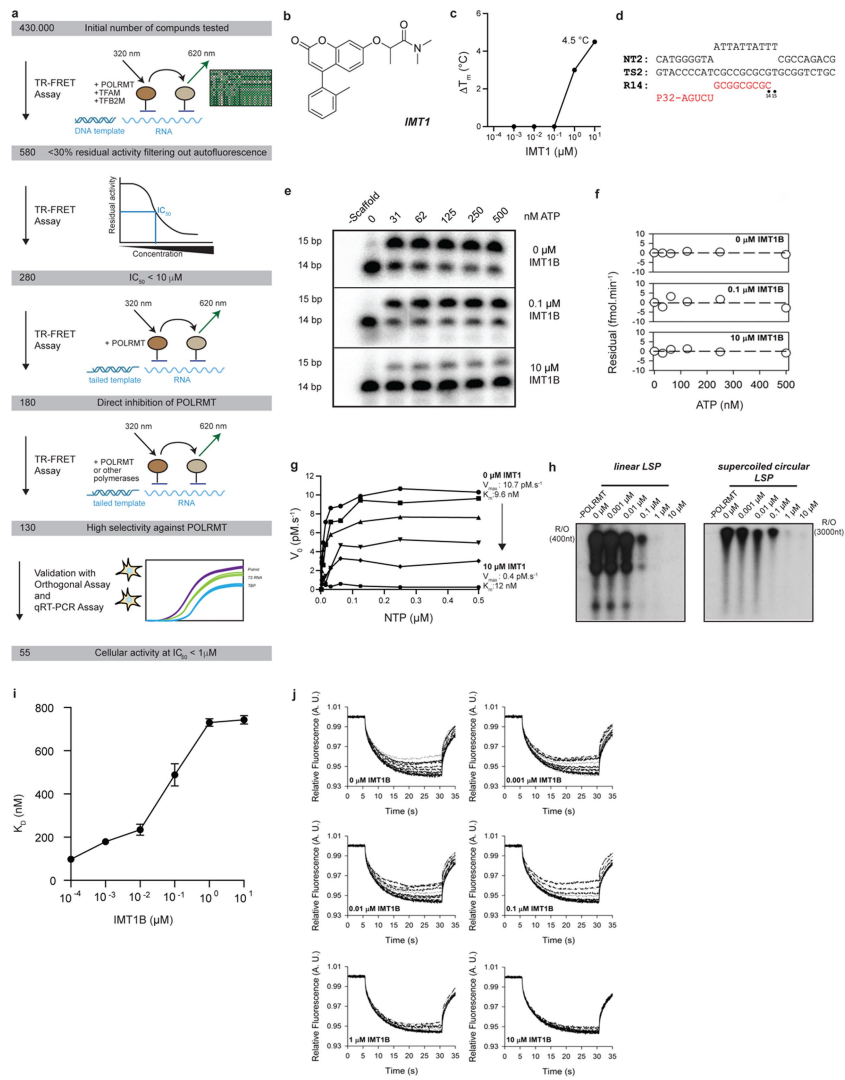
## Additional information

**Supplementary information** is available for this paper at <https://doi.org/10.1038/s41586-020-03048-z>.

**Correspondence and requests for materials** should be addressed to C.M.G. or N.-G.L.

**Peer review information** *Nature* thanks Navdeep Chandel, Angela Koehler and the other, anonymous, reviewer(s) for their contribution to the peer review of this work. Peer reviewer reports are available.

**Reprints and permissions information** is available at <http://www.nature.com/reprints>.

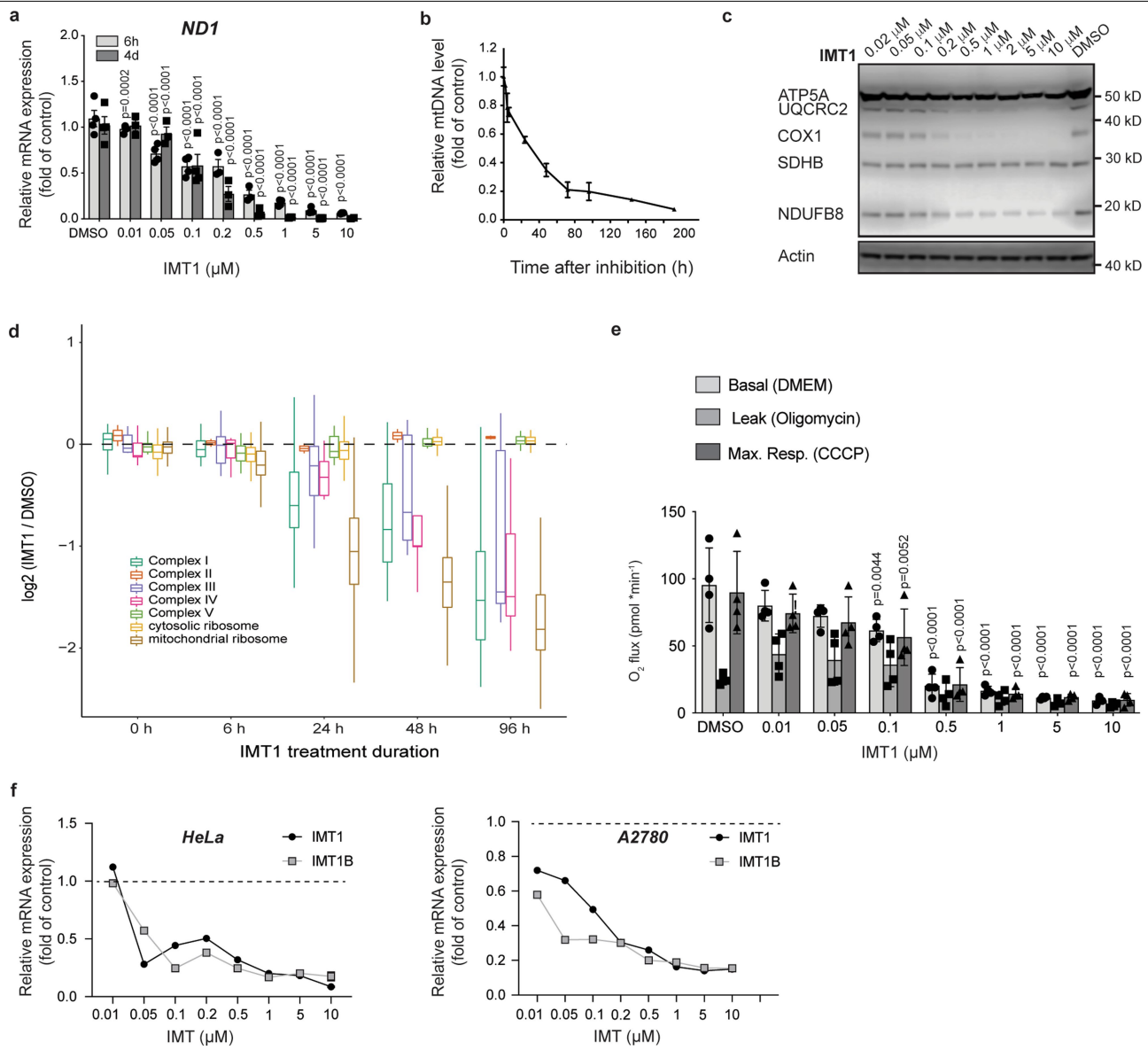


### Extended Data Fig. 1 | IMT1 affects POLRMT stability and DNA binding.

**a**, Overview of the high-throughput screening procedure for IMTs. **b**, Chemical structure of IMT1 (LDC195943). **c**, Differential scanning fluorimetry performed in the presence IMT1. The shift in melting temperature ( $\Delta T_m$ ) is plotted against the IMT1 concentration ( $n = 2$  independent experiments). **d**, Template used in the single ribonucleotide incorporation and MST assays. NT2, non-template strand; TS2, template strand; R14, 14-mer RNA. **e**, Representative gels used for the determination of Michaelis–Menten kinetics in Fig. 1c. The P32-labelled 14-mer scaffold and the extended 15-mer product are indicated. A representative image of  $n = 3$  independent experiments is shown. **f**, Residuals

of the fits to the steady-state POLRMT kinetics data. **g**, Single nucleotide incorporation at varying substrate concentrations in the presence of 0–10  $\mu M$  IMT1 (mean values of  $n = 2$  independent experiments). **h**, In vitro promoter-dependent transcription on linear LSP and supercoiled circular LSP templates in the presence of 0–10  $\mu M$  IMT1. A representative image of  $n = 2$  independent experiments is shown. Quantification is shown in Fig. 1d. **i**, A concentration-dependent decrease in binding affinity ( $K_d$ ) was observed between POLRMT and a RNA–DNA scaffold at increasing levels of IMT1 (mean  $\pm$  s.d.,  $n = 3$  independent experiments). **j**, Raw MST traces.

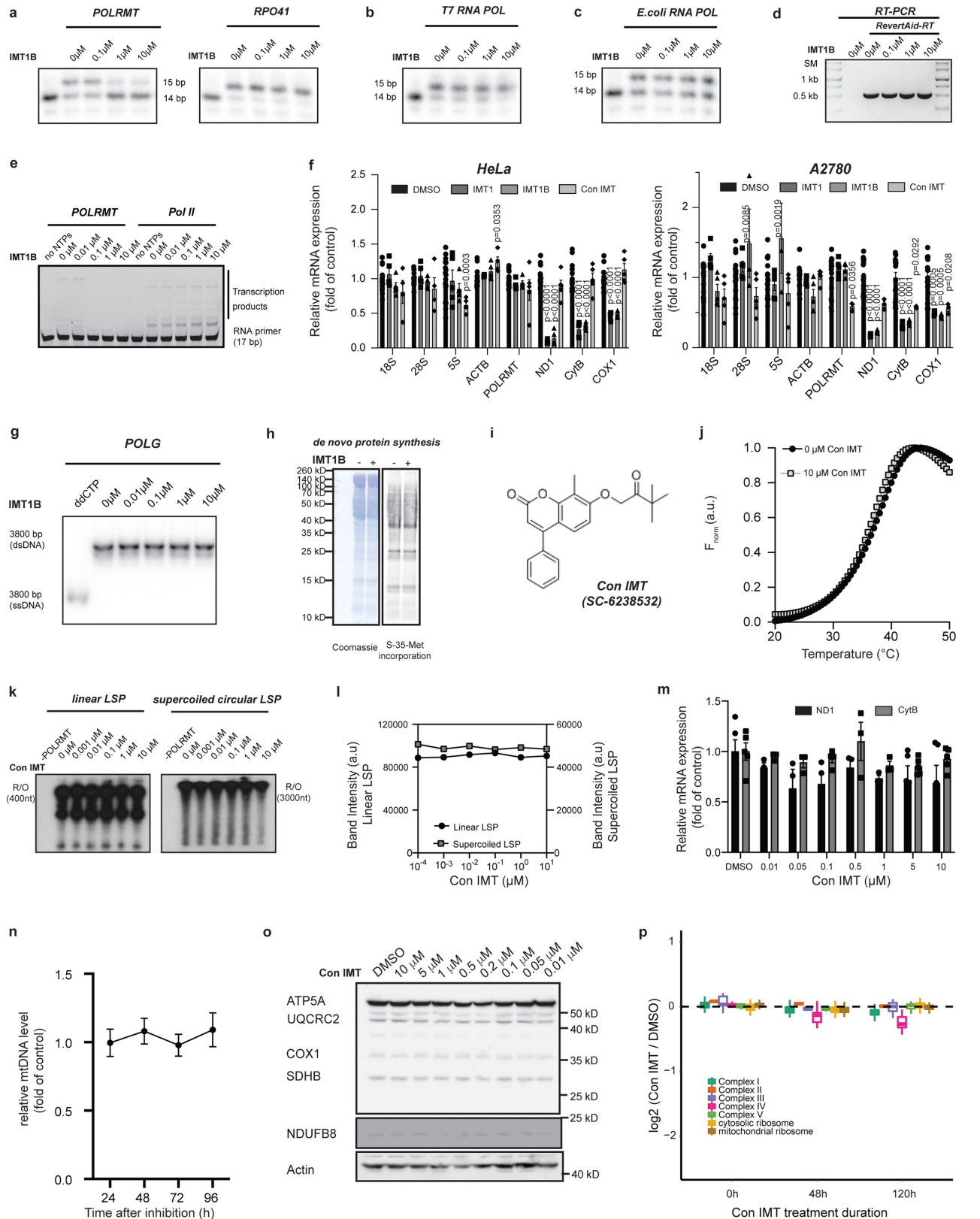
# Article



## Extended Data Fig. 2 | IMT1 affects mitochondrial gene expression.

**a**, Mitochondrial transcript levels of *ND1* after 6 h and 4 d of IMT1 treatment (mean ± s.e.m.,  $n = 3$ –4 biological replicates, two-way ANOVA, Sidak's multiple comparisons test, DMSO–IMT1). **b**, mtDNA levels after IMT1 treatment (mean ± s.e.m.,  $n = 3$  (144 h, 192 h), 4 (4 h, 6 h, 96 h), 6 (24 h, 48 h, 72 h) or 8 (DMSO) biological replicates). **c**, Immunoblot analysis of OXPHOS protein levels after IMT1 treatment (30 μg per lane). A representative image of  $n = 3$  independent experiments is shown. **d**, Quantitative proteomics of IMT1 treatment over time ( $n = 5$  biological replicates). Within each time point, IMT-treated samples were compared to control samples (DMSO). Changes in the protein levels of OXPHOS complexes, mitoribosomal subunits and

cytosolic ribosomes are plotted as log<sub>2</sub>-transformed change in abundance relative to control over time. The exact values for median, upper and lower box hinge and upper and lower whiskers are shown in Supplementary Table 6 (compound IMT1). **e**, Intact cell respiration in HeLa cells after IMT1 exposure. Basal respiration, leak respiration and maximum respiration was determined (mean ± s.e.m.;  $n = 4$  independent measurements, two-way ANOVA, Sidak's multiple comparisons test, respective DMSO control–IMT1). **f**, Comparison of *ND1* transcript levels after IMT1 (Extended Data Fig. 2a) and IMT1B (Fig. 1f) treatment in HeLa and A2780 cells. Dashed lines indicate *ND1* transcript levels in DMSO-treated controls.

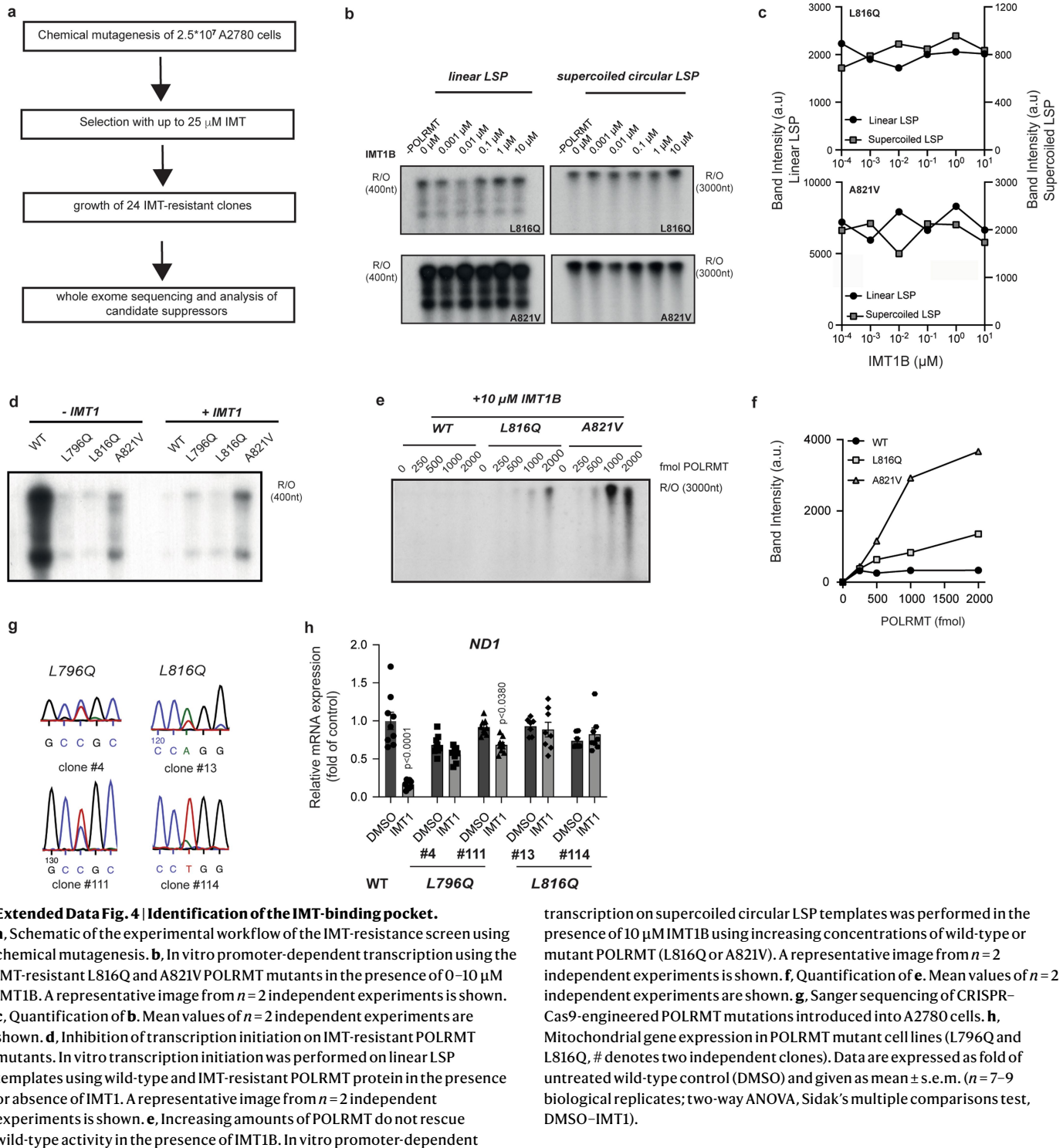


**Extended Data Fig. 3** | See next page for caption.

# Article

**Extended Data Fig. 3 | IMTs are highly specific.** **a–c**, Single ribonucleotide incorporation assay using the template displayed in Extended Data Fig. 1d. IMT1B inhibits POLRMT, but does not affect RPO41 (**a**), T7 RNA polymerase (**b**) or *E. coli* RNA polymerase (**c**). The first lane in each panel is template only, without added enzyme. Representative images from  $n=3$  independent experiments are shown. **d**, IMT1B does not inhibit cDNA synthesis by RevertAid reverse transcriptase. Reverse transcriptase was omitted in the second lane. A representative image from  $n=3$  independent experiments is shown. **e**, Primer extension assay of POLRMT and RNA polymerase II performed in the presence of increasing concentrations of IMT1B. A representative image from  $n=3$  independent experiments is shown. **f**, IMT treatment does not affect the expression of nuclear RNA polymerase targets. HeLa and A2780 cells were treated with either DMSO or IMT1, IMT1B and a commercially available IMT (con IMT) used as a control. mRNA levels of polymerase targets (RNA Pol I: 18S, 28S; RNA Pol II: POLRMT,  $\beta$ -actin; RNA Pol III: 5S; POLRMT: ND1, CYTB, COX1) are given as mean  $\pm$  s.e.m. ( $n=4$  (con IMT) or 5 (IMT1, IMT1B) biological replicates, two-way ANOVA, Sidak's multiple comparisons test, DMSO–respective IMT treatment). **g**, IMT1B does not inhibit POLy primer elongation. The input template for POLy is 3,800-nt single-stranded DNA that becomes a 3,800-bp nicked circular template product when synthesized. A representative image from  $n=3$  independent experiments is shown. First lane, ddCTP control. **h**, In organello translation of freshly isolated mitochondria in the presence or

absence of IMT1B. A representative image from  $n=2$  biological replicates is shown. **i**, Chemical structure of con IMT (SC-6238532), a structurally related analogue of IMTs. **j**, Differential scanning fluorimetry performed in the presence or absence of con IMT ( $n=2$  independent experiments). **k**, In vitro promoter-dependent transcription on linear LSP and supercoiled circular LSP templates was performed in the presence of 0–10  $\mu$ M con IMT. A representative image from  $n=2$  independent experiments is shown. R/O, run-off transcript. **l**, Quantification of **k**. Mean values of  $n=2$  independent experiments are shown. **m**, Mitochondrial transcript levels of ND1 and CYTB determined after treatment of HeLa cells with different concentrations of con IMT for 6 h (mean  $\pm$  s.e.m.,  $n=3, 4$  (0.1  $\mu$ M) or 5 (DMSO, 10  $\mu$ M, 5  $\mu$ M) biological replicates). **n**, mtDNA levels in HeLa cells treated with con IMT (mean  $\pm$  s.e.m.,  $n=3, 4$  (72 h) or 5 (DMSO) biological replicates). **o**, Immunoblot analysis of OXPHOS protein levels in HeLa cells treated with Con IMT for 4 d (20  $\mu$ g per lane). A representative image from  $n=2$  independent experiments is shown. **p**, Quantitative proteomics of con IMT treatment over time ( $n=5$  biological replicates). Within each time point, treated samples were compared to control samples (DMSO). Changes in the protein levels of OXPHOS complexes, mitoribosomal subunits and cytosolic ribosomes are plotted as  $\log_2$ -transformed change in abundance relative to control over time. The exact values for median, upper and lower box hinge and upper and lower whiskers are shown in Supplementary Table 6 (compound con IMT).

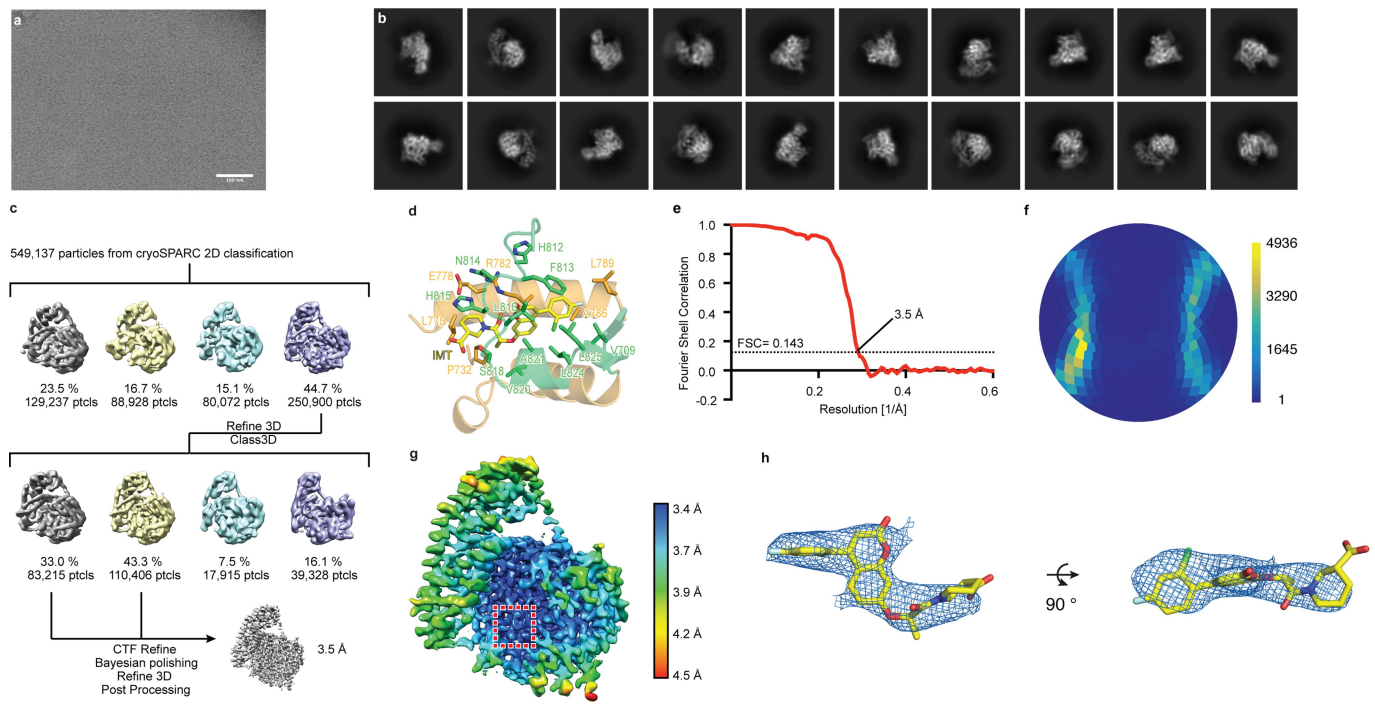


#### Extended Data Fig. 4 | Identification of the IMT-binding pocket.

**a**, Schematic of the experimental workflow of the IMT-resistance screen using chemical mutagenesis. **b**, In vitro promoter-dependent transcription using the IMT-resistant L816Q and A821V POLRMT mutants in the presence of 0–10 μM IMT1B. A representative image from  $n=2$  independent experiments is shown. **c**, Quantification of **b**. Mean values of  $n=2$  independent experiments are shown. **d**, Inhibition of transcription initiation on IMT-resistant POLRMT mutants. In vitro transcription initiation was performed on linear LSP templates using wild-type and IMT-resistant POLRMT protein in the presence or absence of IMT1. A representative image from  $n=2$  independent experiments is shown. **e**, Increasing amounts of POLRMT do not rescue wild-type activity in the presence of IMT1B. In vitro promoter-dependent

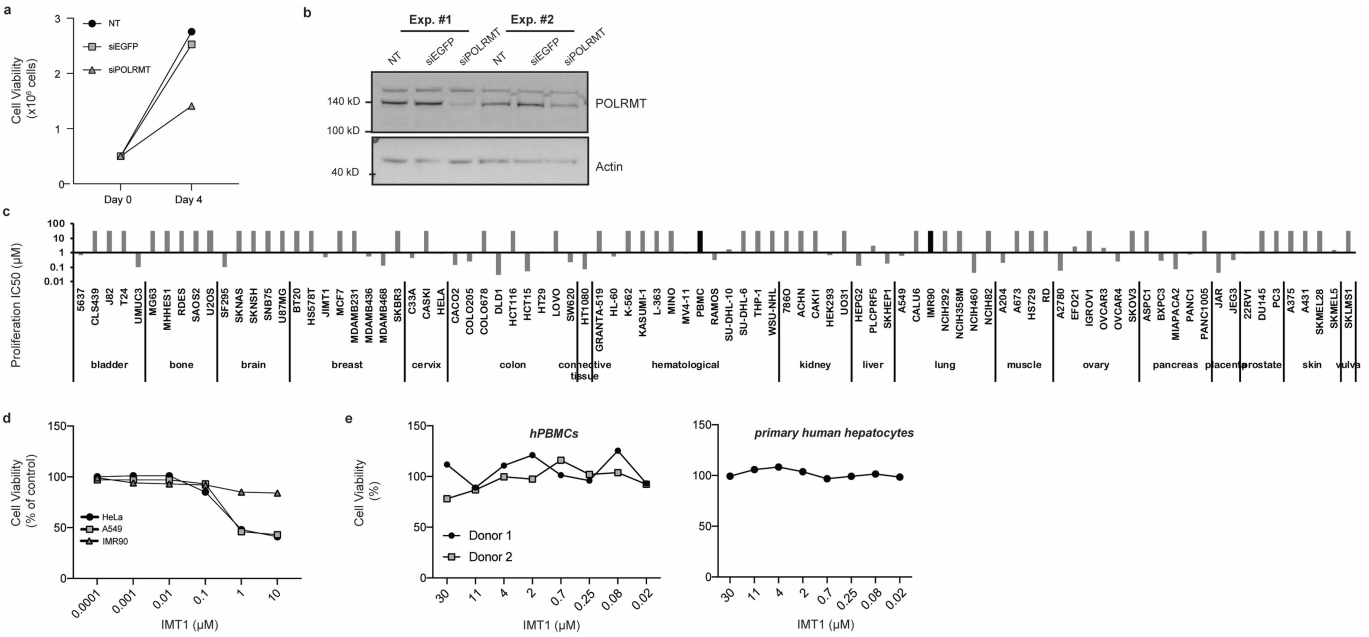
transcription on supercoiled circular LSP templates was performed in the presence of 10 μM IMT1B using increasing concentrations of wild-type or mutant POLRMT (L816Q or A821V). A representative image from  $n=2$  independent experiments is shown. **f**, Quantification of **e**. Mean values of  $n=2$  independent experiments are shown. **g**, Sanger sequencing of CRISPR-Cas9-engineered POLRMT mutations introduced into A2780 cells. **h**, Mitochondrial gene expression in POLRMT mutant cell lines (L796Q and L816Q, # denotes two independent clones). Data are expressed as fold of untreated wild-type control (DMSO) and given as mean  $\pm$  s.e.m. ( $n=7$ –9 biological replicates; two-way ANOVA, Sidak's multiple comparisons test, DMSO–IMT1).

# Article



**Extended Data Fig. 5 | Structure determination of POLRMT with IMT1B by cryo-EM.** **a**, Representative micrograph from 40° tilted data collection ( $n=2,077$  micrographs). **b**, Most populated classes from 2D classification using cryoSPARC 6. **c**, Cryo-EM processing workflow. **d**, Binding pocket of IMT1B between the POLRMT thumb and palm domains. POLRMT is shown as a translucent cartoon, and residues within 4 Å of IMT1B are shown as sticks.

IMT1B was modelled on the basis of the cryo-EM density and chemical considerations (Methods). **e**, Fourier shell correlation plot. **f**, Angular distribution of particle views. **g**, Local resolution estimation calculated using RELION 3. The position of IMT1B is indicated with a red dashed box. **h**, Cryo-EM density around IMT1B. IMT1B is shown as sticks, and the cryo-EM density is shown as blue mesh with a carve of 2 Å.

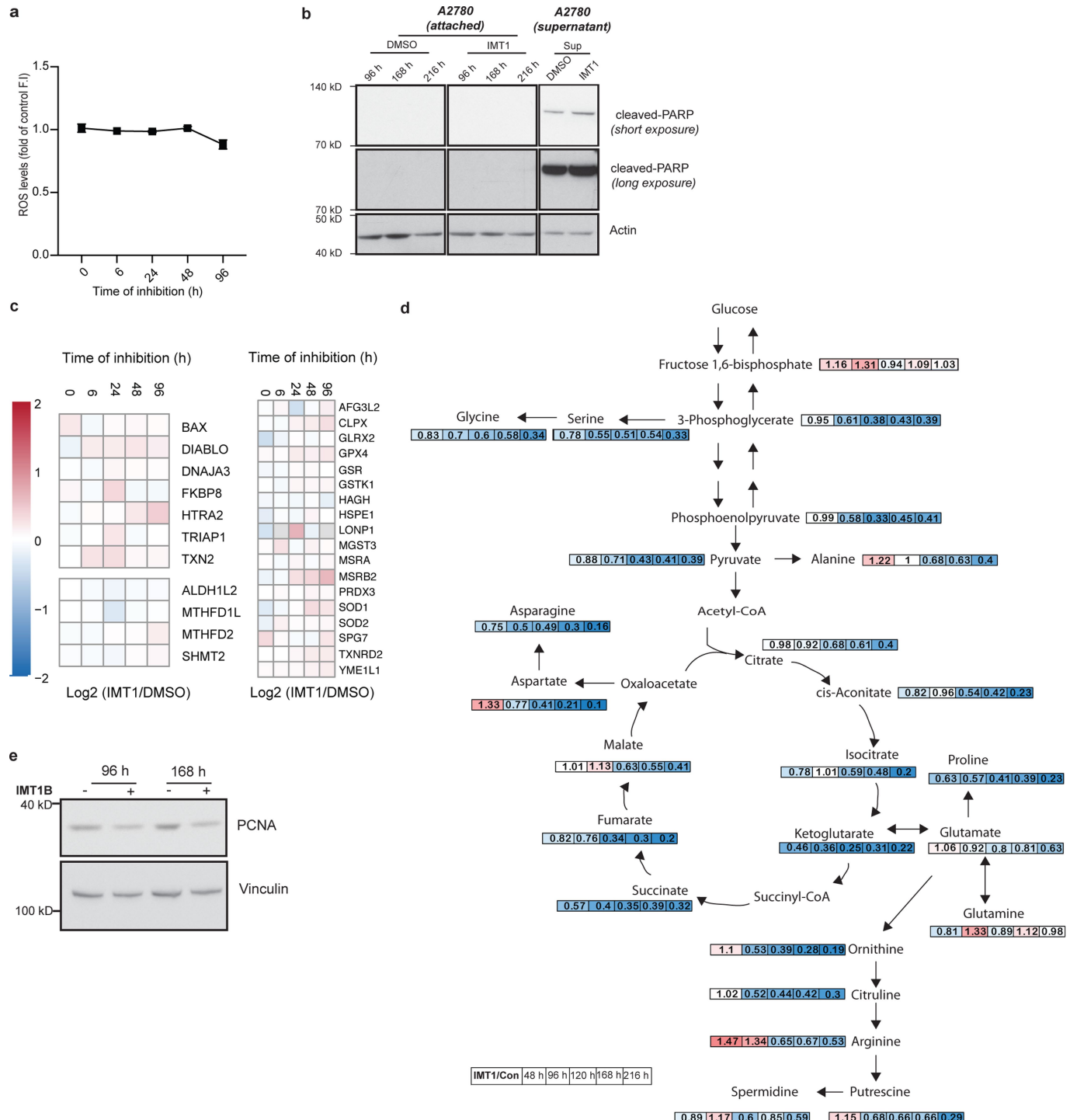


#### Extended Data Fig. 6 | Loss of POLRMT leads to a decrease in cell viability.

**a**, POLRMT silencing in HeLa cells affects cell viability. Cell viability was assessed using a ViCell Cell counter. Mean of  $n=2$  independent experiments is shown. NT, non-transfected. **b**, Immunoblot analysis of POLRMT levels 4 d after transfection (20  $\mu$ g per lane). A representative image of  $n=2$  independent experiments is shown. **c**, Analysis of cancer cell proliferation using an SRB proliferation assay indicates that IMT1 treatment specifically inhibits cancer cell proliferation in a variety of cancer cell lines, but not in control cells.  $IC_{50}$

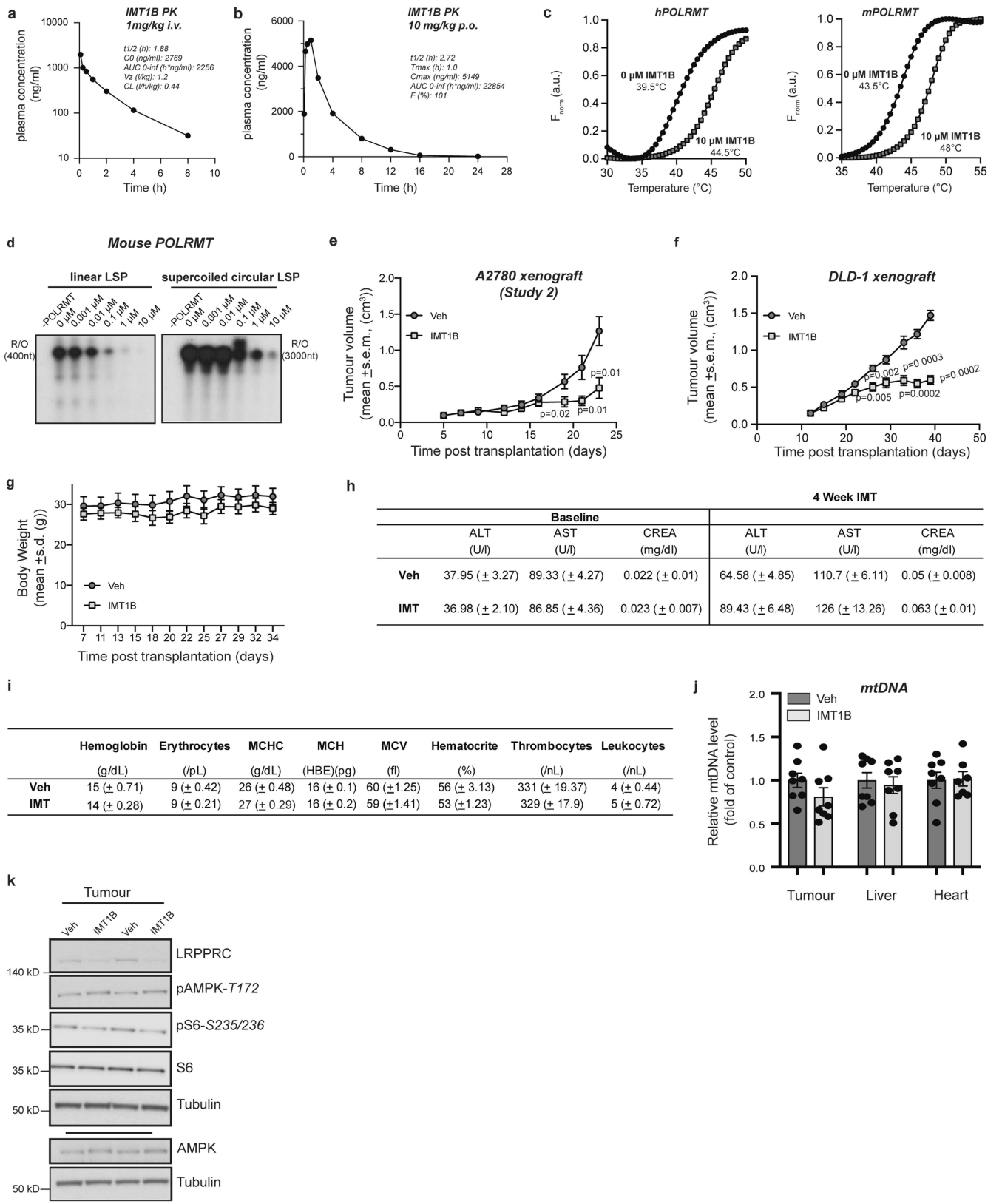
values of IMT1 on a panel of 89 cancer cell lines (grey) and primary cells (black, IMR90 lung fibroblasts and human PBMCs) are plotted. **d**, Cell growth in HeLa cells ( $IC_{50}=0.838 \mu\text{M}$ ), lung carcinoma cells (A594) ( $IC_{50}=0.643 \mu\text{M}$ ) and IMR90 lung fibroblast cells ( $IC_{50}>30 \mu\text{M}$ ) after IMT1 treatment was assessed using an SRB assay. **e**, Cytotoxicity against human (h)PBMCs (two different donors, left) or primary human hepatocytes (right) was assessed using the CellTiter-Glo assay at the indicated inhibitor concentrations ( $n=2$  independent experiments).

# Article



**Extended Data Fig. 7 | Basis of IMT-induced cellular toxicity.** **a**, ROS levels after IMT1 treatment in A2780 cells were determined using the Cellular ROS assay kit Orange (mean  $\pm$  s.e.m.,  $n=5$  biological replicates). **b**, Immunoblot analysis of the apoptosis marker cleaved PARP. A2780 cells were treated with IMT1 for the indicated time points and collected by trypsin treatment (attached). For later time points, cell culture supernatants were collected and detached or dead cells were isolated by centrifugation (supernatant) (20  $\mu$ g per lane). A representative image of  $n=3$  independent experiments is shown.

**c**, Heat maps illustrating the fold-change in protein levels in apoptosis (top, left), one-carbon pathway (bottom, left), degradation and stress response (right). **d**, Overview of changes in central carbon metabolism after IMT1 treatment. Changes in metabolite levels are given as fold of control at the indicated time points. Dark blue, minimum (0); dark red, maximum (2). **e**, Immunoblot analysis of the proliferation marker PCNA. A2780 cells were treated with IMT1B (+) or DMSO (-) for the indicated time points (20  $\mu$ g per lane). A representative image of  $n=2$  independent experiments is shown.



**Extended Data Fig. 8** | See next page for caption.

# Article

**Extended Data Fig. 8 | IMT treatment in vivo.** **a, b**, Pharmacokinetic (PK) parameters of IMT1B used in the in vivo studies: intravenous dosing (**a**) or oral dosing (**b**) ( $n=3$  biological replicates).  $t_{1/2}$ , elimination half-life;  $T_{max}$ , time to reach peak plasma concentration following drug administration (that is,  $C_{max}$ );  $C_0$ , concentration extrapolated to the origin;  $C_{max}$ , peak plasma drug concentration; AUC 0–inf, area under the plasma concentration time curve from time zero to infinity;  $V_z$ , volume of distribution; CL, total plasma clearance;  $F$ , bioavailability. **c**, Mouse POLRMT is stabilized by IMT1B. Differential scanning fluorimetry performed in the presence or absence of IMT1B using human (left) or mouse (right) POLRMT ( $n=2$  independent experiments). The determined melting temperatures are given. **d**, IMT1B inhibits promotor-dependent transcription using mouse POLRMT in a concentration-dependent manner in vitro. In vitro promoter-dependent transcription on linear LSP and supercoiled circular LSP templates was performed in the presence of 0–10  $\mu$ M IMT1B. A representative image of  $n=2$  independent experiments is shown. **e**, A2780 xenograft tumour growth in vivo (study 2). Mice were treated once per day with either vehicle (veh) or IMT1B (100 mg kg $^{-1}$ ). Mean  $\pm$  s.e.m.;  $n=8$  biological replicates, Mann–Whitney  $U$  test, exact significance, one-tailed, vehicle–IMT1B. **f**, IMT1B treatment inhibits DLD-1 xenograft tumour growth in vivo. Mice were treated once per day with either vehicle or IMT1B (100 mg kg $^{-1}$ ). Mean  $\pm$  s.e.m.,  $n=8$  biological replicates, Mann–Whitney  $U$  test, exact significance, one-tailed, vehicle–IMT1B. **g**, Mean

body weight of IMT1B-treated mice in comparison to vehicle-treated controls in the A2780 xenografts. Mean  $\pm$  s.e.m.,  $n=8$  biological replicates. **h**, IMT1B treatment induces no acute liver or kidney toxicity after four weeks of treatment. NMRI mice were treated with either vehicle or IMT1B for four weeks orally once per day. Blood was taken after fasting at the first day (baseline) and last day (4 weeks IMT) of treatment from the tail vein. Blood parameters analysed include alanine transaminase levels (ALT, in U l $^{-1}$ ) and aspartate aminotransferase (AST, in U l $^{-1}$ ) to determine liver toxicity as well as creatinine (CREA, in mg dl $^{-1}$ ) to determine kidney toxicity. Data are presented as mean  $\pm$  s.e.m.,  $n=4$  biological replicates. **i**, IMT1B treatment does not affect blood count after IMT treatment. Female NMRI mice were treated with either vehicle or IMT1B for four weeks orally once per day. Blood was taken on the last day of the experiments and analysed for the abovementioned parameters. Data are presented as mean  $\pm$  s.e.m.,  $n=4$  biological replicates. MCHC, mean corpuscular haemoglobin concentration; MCH, mean corpuscular haemoglobin; MCV, mean corpuscular volume. **j**, Mitochondrial DNA levels in tumour, liver and heart (mean  $\pm$  s.e.m.,  $n=8$  biological replicates). **k**, Immunoblot analysis of phosphorylated AMPK and ribosomal S6 protein levels in tumour tissue lysates. For determination of total AMPK levels, samples were run on a separate gel and processed in parallel (20  $\mu$ g per lane). A representative image of  $n=3$  independent experiments is shown.

Corresponding author(s): N.G. Larsson

Last updated by author(s): Oct 6, 2020

## Reporting Summary

Nature Research wishes to improve the reproducibility of the work that we publish. This form provides structure for consistency and transparency in reporting. For further information on Nature Research policies, see [Authors & Referees](#) and the [Editorial Policy Checklist](#).

### Statistics

For all statistical analyses, confirm that the following items are present in the figure legend, table legend, main text, or Methods section.

n/a Confirmed

- The exact sample size ( $n$ ) for each experimental group/condition, given as a discrete number and unit of measurement
- A statement on whether measurements were taken from distinct samples or whether the same sample was measured repeatedly
- The statistical test(s) used AND whether they are one- or two-sided  
*Only common tests should be described solely by name; describe more complex techniques in the Methods section.*
- A description of all covariates tested
- A description of any assumptions or corrections, such as tests of normality and adjustment for multiple comparisons
- A full description of the statistical parameters including central tendency (e.g. means) or other basic estimates (e.g. regression coefficient) AND variation (e.g. standard deviation) or associated estimates of uncertainty (e.g. confidence intervals)
- For null hypothesis testing, the test statistic (e.g.  $F$ ,  $t$ ,  $r$ ) with confidence intervals, effect sizes, degrees of freedom and  $P$  value noted  
*Give  $P$  values as exact values whenever suitable.*
- For Bayesian analysis, information on the choice of priors and Markov chain Monte Carlo settings
- For hierarchical and complex designs, identification of the appropriate level for tests and full reporting of outcomes
- Estimates of effect sizes (e.g. Cohen's  $d$ , Pearson's  $r$ ), indicating how they were calculated

*Our web collection on [statistics for biologists](#) contains articles on many of the points above.*

### Software and code

Policy information about [availability of computer code](#)

Data collection

NanoTemper analysis software; QuantStudio 6 Flex Real-time qPCR software

Data analysis

In addition to abovementioned tools also used for analysis, the following software was used: SigmaPlot (v.11.0.); GraphPad Prism (v.8.0); PKSolver Plugin for MicrosoftExcel (v.2.0); Warp (v.1.0.7.); cryoSPARC (v.2.14.2); Relion (v.3.0.7); Coot (v.0.9.); Phenix (v.1.18); FreeStyle (v.1.6); MaxQuant (v.1.6.10.43); R-Studio (v.1.1.383.); TraceFinder (v.4.1); Progenesis QI Software (v.2.3); TargetLynx Software (v.4.1 SCN 950)

For manuscripts utilizing custom algorithms or software that are central to the research but not yet described in published literature, software must be made available to editors/reviewers. We strongly encourage code deposition in a community repository (e.g. GitHub). See the Nature Research [guidelines for submitting code & software](#) for further information.

### Data

Policy information about [availability of data](#)

All manuscripts must include a [data availability statement](#). This statement should provide the following information, where applicable:

- Accession codes, unique identifiers, or web links for publicly available datasets
- A list of figures that have associated raw data
- A description of any restrictions on data availability

The central data generated and analysed during this study are included in this article. Source data used to generate graphs are provided with this manuscript. Uncropped gels can be found in Supplemental Figure 1. Publicly available datasets used in this study are: human proteome database (UP000005640, Uniprot), POLRMT structures (PDB IDs: 5OLA, 4BOC, Protein Data Bank). Further information and requests for unique reagents should be directed to the corresponding authors. Proteomics data and R scripts for analysis were deposited into PRIDE with the dataset identifier PXD018426. The electron microscopy maps were deposited with the Electron Microscopy Data Bank (accession code EMD-11679) and the structural model of POLRMT with IMT1B was deposited with the Protein Data Bank (accession code 7A8P).

# Field-specific reporting

Please select the one below that is the best fit for your research. If you are not sure, read the appropriate sections before making your selection.

- Life sciences       Behavioural & social sciences       Ecological, evolutionary & environmental sciences

For a reference copy of the document with all sections, see [nature.com/documents/nr-reporting-summary-flat.pdf](http://nature.com/documents/nr-reporting-summary-flat.pdf)

## Life sciences study design

All studies must disclose on these points even when the disclosure is negative.

Sample size	In vitro, cell culture and metabolomics experiments were performed using sample sizes based on standard protocols in the field. For quantitative proteomics, we chose a sample size which we determined previously to be a highly reproducible value. For tumour xenograft studies, sample sizes were pre-determined by statistical analysis. For toxicity and pharmacokinetic panels, no sample size determination was performed, cohort sizes were chosen based on previous experience to balance an exploratory, observational study with needless use of excess animals.
Data exclusions	For qPCR tissue analysis, samples were excluded if there was no sufficient amount of starting material (RNA, DNA) to perform the standardized experiment. In mouse tumour volume analysis, no samples were excluded.
Replication	All experimental data was reliably reproduced as indicated in the method section and figure legends. For mouse xenograft studies, one independent DLD1 xenograft study and three independent A2780 xenograft studies were conducted, two of which are shown here. All of the tumor xenograft studies showed similar results. For toxicity panels and pharmacokinetics, one independent study was performed.
Randomization	Tumour-bearing mice were randomly allocated to treatment groups. For toxicity studies, mice were weighed and groups assigned according to a randomized block design such that mean starting weight was similar in all groups.
Blinding	For mouse studies, investigators were not blinded to group allocation or experimental outcome, as the compound was not provided blinded. Investigators were also not blinded during sample analysis.

## Reporting for specific materials, systems and methods

We require information from authors about some types of materials, experimental systems and methods used in many studies. Here, indicate whether each material, system or method listed is relevant to your study. If you are not sure if a list item applies to your research, read the appropriate section before selecting a response.

Materials & experimental systems		Methods	
n/a	Involved in the study	n/a	Involved in the study
<input type="checkbox"/>	<input checked="" type="checkbox"/> Antibodies	<input checked="" type="checkbox"/>	ChIP-seq
<input type="checkbox"/>	<input checked="" type="checkbox"/> Eukaryotic cell lines	<input checked="" type="checkbox"/>	Flow cytometry
<input checked="" type="checkbox"/>	<input type="checkbox"/> Palaeontology	<input checked="" type="checkbox"/>	MRI-based neuroimaging
<input type="checkbox"/>	<input checked="" type="checkbox"/> Animals and other organisms		
<input checked="" type="checkbox"/>	<input type="checkbox"/> Human research participants		
<input checked="" type="checkbox"/>	<input type="checkbox"/> Clinical data		

## Antibodies

Antibodies used	Total OXPHOS Rodent WB Antibody Cocktail (ab110413, Abcam); anti-actin (ab3280, Abcam); anti-MTCO1 (ab14705, Abcam); anti-phospho-AMPK (T172) (#2535, Cell Signalling Technology); anti-AMPK (#2532, Cell Signalling Technology); anti-phospho-S6 ribosomal protein (#4856, Cell Signalling Technology); anti-S6 ribosomal protein (#2217, Cell Signalling Technology); anti-LRPPRC (AgriSera Cat# LRPPRC_antibody, RRID:AB_2716302); anti-tubulin (#2125, Cell Signalling Technology); anti-tubulin (T9026, Sigma); anti-Vinculin (ab129002, Abcam); anti-HSP60 (#4870; Cell Signalling Technology); anti-hPOLRMT (sc-67350, Santa Cruz, kind gift from D. Temiakov); anti-cleaved PARP (used as part of the Cell Cycle and Apoptosis WB Cocktail, ab139417, Abcam), anti-PCNA (ab29, abcam); anti-mouse IgG (NXA931V, GE Healthcare); anti-rabbit IgG (NA9340V, GE Healthcare)
Validation	<p>Primary antibodies for western blotting:</p> <ul style="list-style-type: none"> <li>- anti-LRPPRC: The self-made antibody against LRPPRC (AgriSera Cat# LRPPRC_antibody, RRID:AB_2716302) has been published previously and was shown to specifically detect LRPPRC by western blotting comparing protein levels in mitochondrial extracts of wild-type and LRPPRC knock-out samples. <a href="https://scicrunch.org/resolver/AB_2716302">https://scicrunch.org/resolver/AB_2716302</a></li> <li>- Total OXPHOS Rodent WB Antibody Cocktail (ab110413, Abcam): The Abpromise covers the use of the antibody for WB application. The antibody has been referenced in 592 publications. <a href="https://www.abcam.com/total-oxphos-rodent-wb-antibody">https://www.abcam.com/total-oxphos-rodent-wb-antibody</a></li> </ul>

cocktail-ab110413.html

- anti-actin (ab3280, Abcam): The Abpromise covers the use of the antibody for WB application. The antibody had been referenced in 399 publications, however, it has been discontinued.
- anti-MTCO1 (ab14705, Abcam): The Abpromise covers the use of the antibody for WB application. The antibody had been referenced in 310 publications. <https://www.abcam.com/mtco1-antibody-1d6e1a8-ab14705.html>
- anti-phospho-AMPK (T172) (#2535, Cell Signalling Technology): The antibody guarantee covers the use of the antibody for WB applications. The antibody has been referenced in 1597 publications. <https://www.cellsignal.com/products/primary-antibodies/phospho-ampka-thr172-40h9-rabbit-mab/2535?Ntk=Products&Ntt=2535>
- anti-AMPK (#2532, Cell Signalling Technology): The antibody guarantee covers the use of the antibody for WB applications. The antibody has been referenced in 1163 publications. <https://www.cellsignal.com/products/primary-antibodies/ampka-antibody/2532?Ntk=Products&Ntt=2532>
- anti-phospho-S6 ribosomal protein (#4856, Cell Signalling Technology): The antibody guarantee covers the use of the antibody for WB applications. The antibody has been referenced in 184 publications. <https://www.cellsignal.com/products/primary-antibodies/phospho-s6-ribosomal-protein-ser235-236-2f9-rabbit-mab/4856?Ntk=Products&Ntt=4856>
- anti-S6 ribosomal protein (# 2217, Cell Signalling Technology): The antibody guarantee covers the use of the antibody for WB applications. The antibody has been referenced in 1087 publications. <https://www.cellsignal.com/products/primary-antibodies/s6-ribosomal-protein-5g10-rabbit-mab/2217?Ntk=Products&Ntt=2217>
- anti-tubulin (#2125, Cell Signalling Technology): The antibody guarantee covers the use of the antibody for WB applications. The antibody has been referenced in 365 publications. <https://www.cellsignal.com/products/primary-antibodies/a-tubulin-11h10-rabbit-mab/2125?Ntk=Products&Ntt=2125>
- anti-tubulin (T9026, Sigma): The antibody was subjected to enhanced antibody validation and referenced in 3026 publications. <https://www.sigmaldrich.com/catalog/product/sigma/t9026?lang=de&region=DE>
- anti-Vinculin (ab129002, Abcam): The Abpromise covers the use of the antibody for WB application. The antibody had been referenced in 105 publications. <https://www.abcam.com/vinculin-antibody-epr8185-ab129002.html>
- anti-HSP60 (#4870; Cell Signalling Technology): The antibody guarantee covers the use of the antibody for WB applications. The antibody has been referenced in 60 publications. <https://www.cellsignal.de/products/primary-antibodies/hsp60-d307-antibody/4870?Ntk=Products&Ntt=4870>
- anti-hPOLRMT (sc-67350, Santa Cruz): The antibody has been verified using siRNA knockdown of POLRMT in HeLa cells (Kühl, 2014 and this study), recombinant hPOLRMT was loaded as a control (see Supplementary Figure 1). The product seems to have been discontinued.
- anti-cleaved PARP (used as part of the Cell Cycle and Apoptosis WB Cocktail, ab139417, Abcam): The Abpromise covers the use of the antibody for WB application. <https://www.abcam.com/cell-cycle-and-apoptosis-wb-cocktail-pcdkphh3actinparp-ab139417.html>
- anti-PCNA (ab29, abcam): The Abpromise covers the use of the antibody for WB application. The antibody has been referenced in 368 publications. <https://www.abcam.com/pcna-antibody-pc10-ab29.html>

## Eukaryotic cell lines

Policy information about [cell lines](#)

Cell line source(s)

Cell lines were derived from American Type Culture Collection (ATCC), European Collection of Authenticated Cell Cultures (ECACC), Cell Line Service GmbH (CLS), National Institutes of Cancer (NCI-DTP) and DSMZ-German Collection of Microorganisms and Cell Cultures GmbH.

HeLa (ATCC CCL-2), A2780 (ECACC 93112519), DLD-1 (ECACC 90102540), hPBMC (DRK West Blutspendedienst Hagen, Germany), primary human hepatocytes (X008052-P, BioreclamationIVT)

For cell panel: 5637 (ATCC HTB-9), CLS-439 (CLS; 300150), J82 (ATCC HTB-1), T24 (ATCC HTB-4), UMUC3 (ATCC CRL-1749), MG63 (ATCC CRL-1427), MHH-ES1 (CLS; 300136), RD-ES (ATCC HTB-166), SAOS2 (ATCC HTB-85), U2OS (ATCC HTB-96), SF-295 (NCI-DTP, SF-295), SK-N-AS (ATCC CRL-2137), SK-N-SH (ATCC HTB-11), SNB75 (NCI-DTP, SN-75), U87MG (ATCC HTB-14), BT-20 (ATCC HTB-19), Hs578T (ATCC HTB-126), JIMT1 (DSMZ, ACC 589), MCF7 (ATCC HTB-22), MDA-MB-231 (ATCC HTB-26), MDA-MB-436 (ATCC HTB-130), MDA-MB-468 (ATCC HTB-132), SKBR3 (ATCC HTB-30), C33A (ATCC HTB-31), Ca Ski (ATCC CRM-CRL-1550), HeLa (ATCC CCL-2), Caco-2 (ATCC HTB-37), COLO 205 (ATCC CCL-222), COLO-678 (DSMZ, ACC 194), DLD-1 (ECACC,

90102540), HCT-116 (ATCC CCL-247), HCT-15 (ATCC CCL-225), HT-29 (ATCC HTB-38), LoVo (ATCC CCL-229), SW620 (ATCC CCL-227), HT-1080 (ATCC CCL-121), GRANTA-519 (DSMZ, ACC 342), HL-60 (DSMZ, ACC 3), K-562 (DSMZ ACC 10), Kasumi-1 (DSMZ ACC 220), L-363 (DSMZ, ACC 49), Mino (DSMZ, ACC 687), MV-4-11 (DSMZ, ACC 102), PBMC (donor specific), Ramos (DSMZ, ACC 602), SU-DHL-10 (DSMZ, ACC 576), SU-DHL-6 (DSMZ, ACC 572), THP-1 (DSMZ, ACC 16), WSU-NHL (DSMZ, ACC 58), 786-O (ATCC CRL-1932), ACHN (ATCC CRL-1611), Caki-1 (ATCC HTB-46), Hek293 (ATCC CRL-1573), UO-31 (NCI-DTP, UO-31), HepG2 (ATCC HB-8065), PLC/PRF/5 (ATCC CRL-8024), SK-HEP-1 (ATCC HTB-52), A549 (ATCC CCL-185), Calu-6 (ATCC HTB-56), IMR-90 (ATCC CCL-186), NCI-H292 (ATCC CRL-1848), NCI-H358M (NCI-DTP, NCI-H358M), NCI-H460 (ATCC HTB-177), NCI-H82 (ATCC HTB-175), A-204 (ATCC HTB-82), A-673 (ATCC CRL-1598), Hs729 (ATCC HTB-153), RD (ATCC CCL-136), A2780 (ECACC 93112519), EFO-21 (DSMZ, ACC 235), IGROV1 (NCI-DTP, IGR-OV1), OVCAR3 (ATCC HTB-161), OVCAR4 (NCI-DTP, OVCAR-4), SK-OV-3 (ATCC HTB-77), AsPC-1 (ATCC CRL-1682), BxPC-3 (ATCC CRL-1687), MIA PaCa-2 (ATCC CRM-CRL-1420), PANC-1 (ATCC CRL-1469), Panc 10.05 (ATCC CRL-2547), JAR (ATCC HTB-144), JEG-3 (ATCC HTB-36), 22Rv1 (ATCC CRL-2505), DU 145 (ATCC HTB-81), PC-3 (ATCC CRL-1435), A-375 (ATCC CRL-1619), A-431 (ATCC CRL-1555), SK-MEL-28 (ATCC HTB-72), SK-MEL-5 (ATCC HTB-70), SK-LMS-1 (ATCC HTB-88)

## Authentication

All cell lines used here are commercially available and have been verified by the manufacturers by STR analysis of human cell lines.

[https://www.lgcstandards-atcc.org/Products/Cells\\_and\\_Microorganisms/Cell\\_Lines/Misidentified\\_Cell\\_Lines.aspx](https://www.lgcstandards-atcc.org/Products/Cells_and_Microorganisms/Cell_Lines/Misidentified_Cell_Lines.aspx)

<https://www.phe-culturecollections.org.uk/technical/cell-lines-faqs.aspx>

<https://clsgmbh.de/faq.php#2>

<https://dtp.cancer.gov/organization/btb/docs/DCTDTumorRepositoryCatalog.pdf>

<https://www.dsmz.de/collection/catalogue/human-and-animal-cell-lines/identity-control/authentication-of-cell-lines>

## Mycoplasma contamination

Cell lines were routinely examined for mycoplasma contamination (negative).

Commonly misidentified lines  
(See [ICLAC](#) register)

none

**Animals and other organisms**

Policy information about [studies involving animals; ARRIVE guidelines](#) recommended for reporting animal research

## Laboratory animals

Mus musculus: female NMRI:nu/nu, 7-9 weeks; female Balb/c nude (7-9 weeks); male CD-1 (7-9 weeks), male C57Bl6N (10-14 weeks)

## Wild animals

No wild animals were used.

## Field-collected samples

The study does not contain field-collected samples.

## Ethics oversight

Local Animal Welfare authorities: Regional Office for Health and Social Affairs, Berlin; Tübingen Regional Council

Note that full information on the approval of the study protocol must also be provided in the manuscript.